



King's Research Portal

DOI:

[10.1016/j.neuron.2019.11.027](https://doi.org/10.1016/j.neuron.2019.11.027)

Document Version

Peer reviewed version

[Link to publication record in King's Research Portal](#)

Citation for published version (APA):

Namba, T., Dóczi, J., Pinson, A., Xing, L., Kalebic, N., Wilsch-Bräuninger, M., Long, K. R., Vaid, S., Lauer, J., Bogdanova, A., Borgonovo, B., Shevchenko, A., Keller, P., Drechsel, D., Kurzchalia, T., Wimberger, P., Chinopoulos, C., & Huttner, W. B. (2020). Human-Specific ARHGAP11B Acts in Mitochondria to Expand Neocortical Progenitors by Glutaminolysis. *Neuron*, *105*(5), 867-881.e9. <https://doi.org/10.1016/j.neuron.2019.11.027>

Citing this paper

Please note that where the full-text provided on King's Research Portal is the Author Accepted Manuscript or Post-Print version this may differ from the final Published version. If citing, it is advised that you check and use the publisher's definitive version for pagination, volume/issue, and date of publication details. And where the final published version is provided on the Research Portal, if citing you are again advised to check the publisher's website for any subsequent corrections.

General rights

Copyright and moral rights for the publications made accessible in the Research Portal are retained by the authors and/or other copyright owners and it is a condition of accessing publications that users recognize and abide by the legal requirements associated with these rights.

- Users may download and print one copy of any publication from the Research Portal for the purpose of private study or research.
- You may not further distribute the material or use it for any profit-making activity or commercial gain
- You may freely distribute the URL identifying the publication in the Research Portal

Take down policy

If you believe that this document breaches copyright please contact librarypure@kcl.ac.uk providing details, and we will remove access to the work immediately and investigate your claim.

Human-specific ARHGAP11B acts in mitochondria to expand neocortical progenitors by glutaminolysis

**Takashi Namba^{1*}, Judit Dóczy², Anneline Pinson¹, Lei Xing¹, Nereo Kalebic¹, Michaela
5 Wilsch-Bräuninger¹, Katherine R. Long^{1†}, Samir Vaid¹, Janelle Lauer¹, Aliona Bogdanova¹,
Barbara Borgonovo¹, Anna Shevchenko¹, Patrick Keller¹, David Drechsel^{1‡}, Teymuraz
Kurzchalia¹, Pauline Wimberger³, Christos Chinopoulos², Wieland B. Huttner^{1,4*}**

¹Max Planck Institute of Molecular Cell Biology and Genetics, Pfotenhauerstraße 108, D-01307
10 Dresden, Germany.

²Department of Medical Biochemistry, Semmelweis University, Budapest, Tuzolto st. 37-47,
1094, Hungary.

15 ³Technische Universität Dresden, Universitätsklinikum Carl Gustav Carus, Klinik und Poliklinik
für Frauenheilkunde und Geburtshilfe, Dresden, Germany.

⁴Lead Contact

20 *Correspondence to: Takashi Namba (namba@mpi-cbg.de) and Wieland B. Huttner
(huttner@mpi-cbg.de)

Current addresses:

[†]King's College London, London, UK.

25 [‡]Research Institute of Molecular Pathology, Vienna, Austria.

Summary

Human-specific gene *ARHGAP11B* is preferentially expressed in neural progenitors of fetal human neocortex and increases abundance and proliferation of basal progenitors (BPs), which have a key role in neocortex expansion. *ARHGAP11B* has therefore been implicated in the evolutionary expansion of the human neocortex, but its mode of action has been unknown. Here we show that *ARHGAP11B* is imported into mitochondria where it interacts with the adenine nucleotide translocase (ANT) and inhibits the mitochondrial permeability transition pore (mPTP). BP expansion by *ARHGAP11B* requires its presence in mitochondria, and pharmacological inhibition of ANT function or mPTP opening mimic BP expansion by *ARHGAP11B*. Searching for the underlying metabolic basis, we find that BP expansion by *ARHGAP11B* requires glutaminolysis, the conversion of glutamine to glutamate for the TCA cycle. Hence, an *ARHGAP11B*-induced, mitochondria-based effect on BP metabolism that is a hallmark of highly mitotically active cells appears to underlie its role in neocortex expansion.

Keywords

Neocortex; evolution; metabolism; neural progenitor cells

Introduction

The expansion of the human neocortex, specifically the increase in its mass compared to other primates, is one of the hallmarks of hominin evolution, establishing a foundation for our cognitive abilities (Rakic, 2009; Sun and Hevner, 2014). In the search for the genomic basis underlying human neocortex expansion, researchers have focused on genes, notably human-specific genes, that are preferentially expressed in the stem and progenitor cells of the fetal human neocortex (Fiddes et al., 2018; Florio et al., 2015; Florio et al., 2018; Johnson et al., 2015; Pollen et al., 2015; Suzuki et al., 2018). The rationale of this approach has been that a greater, and more prolonged, mitotic activity of cortical stem and progenitor cells (CSPCs) underlies human neocortex expansion (Dehay et al., 2015; Fernandez et al., 2016; Fietz and Huttner, 2011; Lui et al., 2011; Namba and Huttner, 2017; Rakic, 2009). Two principal classes of CSPCs exist, (i) the apical progenitors (APs) residing in the primary germinal zone, the ventricular zone, and (ii) the basal progenitors (BPs) residing in the secondary germinal zone, the subventricular zone. Among the BPs, two major subtypes can be distinguished: basal intermediate progenitors (bIPs) and basal/outer radial glia cells (bRGs). An increase in BP, in particular bRG, abundance has been implicated in the evolutionary expansion of the neocortex, which may pertain to cortical mass, gyrification, or both (Dehay et al., 2015; Fernandez et al., 2016; Fietz and Huttner, 2011; Lui et al., 2011; Namba and Huttner, 2017). The first human-specific gene shown to be preferentially expressed in CSPCs and to increase BP abundance is *ARHGAP11B* (Florio et al., 2015; Florio et al., 2016; Kalebic et al., 2018).

ARHGAP11B arose by a partial duplication of a ubiquitous gene, *ARHGAP11A*, about 5 million years ago (mya). Hence, this duplication happened after the lineage leading to our closest living relatives, the chimpanzees, had segregated from the lineage leading to Neandertals, Denisovans and modern humans (Antonacci et al., 2014; Dougherty et al., 2018; Meyer et al., 2012; Prüfer et al., 2014; Sudmant et al., 2010). *ARHGAP11A* encodes a Rho GTPase activating protein (Rho-GAP) (Kagawa et al., 2013; Zanin et al., 2013). In contrast, *ARHGAP11B*, which contains most of the GAP-domain of *ARHGAP11A*, does not exhibit Rho-GAP activity in vivo, nor does it exert a dominant-negative effect on the Rho-GAP activity of *ARHGAP11A* (Florio et al., 2015). Moreover, whereas *ARHGAP11B* has been shown to increase BP abundance (bIPs in mouse and bIPs and bRGs in ferret) and to elicit hallmarks of neocortical expansion when expressed in developing mouse and ferret neocortex (Florio et al., 2015; Florio et al., 2016; Kalebic et al., 2018), *ARHGAP11A* is unable to increase BP abundance when expressed in embryonic mouse neocortex (Florio et al., 2015). Remarkably, the ability of *ARHGAP11B* to increase BP abundance is not intrinsic to the protein encoded by the gene as it arose by partial gene duplication 5 mya, but is based on a single C→G nucleotide substitution that likely occurred later in human evolution (Florio et al., 2016). This substitution generates a new splice donor site, resulting in the loss of 55 nucleotides upon mRNA splicing, a reading-frame shift and the generation of a novel 47 amino acid-long C-terminal sequence that is human-specific (referred to as 11B-specific domain) (Florio et al., 2016).

In light of the key role of *ARHGAP11B* in the development and evolutionary expansion of the neocortex as revealed by its effects in animal model systems (Florio et al., 2015; Florio et al., 2016; Kalebic et al., 2018), it is a fundamental challenge to elucidate its mode of action, notably the differences to *ARHGAP11A* and the role of the 11B-specific domain. As an entry point

towards this goal, we have studied the subcellular localization of the ARHGAP11B protein.

Surprisingly, we find that ARHGAP11B is localized in mitochondria and thus shows a subcellular localization distinct from ARHGAP11A, which is found in the nucleoplasm. Within mitochondria, ARHGAP11B interacts with the adenine nucleotide translocase (ANT) in the inner mitochondrial membrane and, via the 11B-specific domain, inhibits the mitochondrial permeability transition pore (mPTP). This mitochondrial action of ARHGAP11B results in an increased use of glutaminolysis, which is found to be essential for BP expansion by ARHGAP11B and which is known to be characteristic of highly mitotically active cells.

Results

ARHGAP11B, expressed in progenitors of fetal human neocortex, is localized in mitochondria, unlike ARHGAP11A

5

To study the molecular function of the ARHGAP11B (11B) protein, we first examined its subcellular localization. To this end, mouse fibroblast cells (NIH-3T3) were transfected with plasmids encoding *ARHGAP11A* (11A) or *11B* (**Figure 1A-C**). By immunofluorescence, 11A was found in the nucleus (**Figure 1B**), as observed previously (Zanin et al., 2013). Surprisingly, however, using a novel, validated (see supplementary materials) monoclonal antibody (mAb) directed against the 11B-specific C-terminal domain (Florio et al., 2015; Florio et al., 2016), 11B was not found in the nucleus but exhibited a cytoplasmic localization. The latter was found to reflect the specific localization of 11B in or on mitochondria, as revealed by counterstaining with MitoTracker (**Figure 1B, C**).

10

15

We therefore searched for the existence of a mitochondrial targeting sequence in 11B, and identified a potential targeting sequence within its 30 N-terminal amino acids (**Figure 1D**). Deletion of amino acids 2-12 (11B Δ 2-12, **Figure 1A, D, Figure S1A**) partially, and of amino acids 2-21 (11B Δ 2-21, **Figure 1A, D, Figure S1A**) completely, abrogated the mitochondrial localization of 11B upon expression in NIH-3T3 cells (**Figure 1E**), as revealed by counter-immunostaining for TOM20 (translocase of outer membrane), a protein localized in the outer mitochondrial membrane that is involved in the import of cytosolically synthesized proteins into mitochondria (Mokranjac and Neupert, 2009; Wiedemann and Pfanner, 2017). These results

20

indicate that the N-terminal domain of 11B contains a mitochondrial targeting sequence that is required for the mitochondrial localization of 11B. Of note, addition of a triple HA tag to the N-terminus of 11B (HA-11B, **Figure 1A**, **Figure S1A**) also completely abolished its mitochondrial localization upon expression in NIH-3T3 cells (**Figure 1E**), likely due to the negative charge of the HA tag. Hence, studying the subcellular localization of 11B using an antibody against the HA tag rather than an antibody against the 11B-specific C-terminal domain (Florio et al., 2016) would yield misleading results.

We next examined whether the mitochondrial targeting sequence of 11B is sufficient for mitochondrial localization. To this end, we constructed a fusion protein (11B1-30-EGFP) in which the 11B N-terminal sequence is followed by EGFP (**Figure 1F**). 11B1-30-EGFP showed complete co-localization with mitochondria upon expression in NIH-3T3 cells, identified by TOM20 immunofluorescence (**Figure 1G**). Importantly, immunoelectron microscopy revealed 11B1-30-EGFP immunoreactivity over the mitochondrial matrix (**Figure 1H**, **Figure S1B, C**).

These data indicate that the mitochondrial targeting sequence present in the N-terminal domain of 11B is not only required, but also sufficient for mitochondrial localization and is capable of directing at least the N-terminal domain of 11B to the mitochondrial matrix.

Further studies, described in detail in supplementary materials, revealed two reasons why 11A, which contains essentially the same mitochondrial targeting sequence in its N-terminal domain as 11B (Florio et al., 2015; Florio et al., 2016), is not localized in mitochondria but in the nucleus (see supplementary materials). First, 11A contains two nuclear localization signals in the domains C-terminal to the GAP domain that are no longer present in 11B due to (i) the gene duplication giving rise to *11B* comprising only the 5' one third of the coding region of the *11A* gene

(Antonacci et al., 2014; Dougherty et al., 2018) (**Figure S1A**), and (ii) the subsequent splice site mutation giving rise to the modern 11B protein (Dougherty et al., 2018; Florio et al., 2016) (**Figure S1A**). Accordingly, truncated versions of 11A lacking the two nuclear localization signals (11A220, 11A250) were not found in the nucleoplasm but in mitochondria (**Figure S1D**).

5 Second, the protein sequence following the GAP domain in 11A is sterically close to its N-terminal domain (Protein Data Bank [PDB] ID code 3EAP; see also **Figure S1F**) and, when extending beyond amino acid residue 250, likely masks the mitochondrial targeting sequence (**Figure S1A**). Consistent with these considerations, ancestral 11B, which extends beyond amino acid residue 250 and still contains one nuclear localization signal (**Figure S1A**), was found in the
10 nucleoplasm, whereas ancestral 11B with a mutated nuclear localization signal was no longer found in the nucleoplasm but also not yet in mitochondria, but rather in the non-mitochondrial domains of the cytoplasm (**Figure S1E**).

Given that the mitochondrial localization of 11B was so far only shown upon forced expression
15 in mouse NIH-3T3 cells, it was important to corroborate that this localization was also true for the 11B protein physiologically expressed in progenitors of fetal human neocortex. Indeed, using the novel, validated (see supplementary materials) mAb specifically recognizing 11B (**Figure S2A, B**), 11B was found to colocalize with TOM20-immunostained mitochondria in SOX2+ APs in the VZ (**Figure 1I; Figure S2C, compare with Figure S2E, F**) and SOX2+ BPs in the SVZ
20 (**Figure S2C, D, compare with Figure S2E**) of post-conceptual week (PCW) 10 human neocortex. Moreover, both bRGs (TBR2- SOX2+ cells, **Figure S2G**) and bIPs (TBR2+ SOX2+ cells, **Figure S2G**) were found to express the 11B protein. These observations were complemented by analyzing the subcellular localization of 11B upon its forced expression, along with GFP, by *in utero* electroporation (IUE) of embryonic day (E) 13.5 mouse neocortex. Again,

11B was found to colocalize with TOM20-immunostained mitochondria in GFP⁺ cells in the VZ and SVZ of E14.5 mouse neocortex (**Figure 1J**).

The mitochondrial localization of 11B is required for BP expansion

5

We exploited our observations that deletion of the mitochondrial targeting sequence from 11B or addition of an N-terminal triple HA tag would misdirect 11B to cytoplasmic localizations other than mitochondria, to examine whether the mitochondrial localization of 11B is required for its ability to increase BP abundance (Florio et al., 2015; Florio et al., 2016). Forced expression of 11B, along with GFP, by IUE of E13.5 mouse neocortex resulted, at E14.5, in a \approx 2-fold increase (i) in the abundance of basal mitotic (phosphohistone H3⁺ (PH3⁺)) GFP⁺ cells (**Figure 2A, B**), as described previously (Florio et al., 2015; Florio et al., 2016), (ii) in the proportion of GFP⁺ cells that were PH3⁺ and showed a basal location (**Fig. 2A, C**), (iii) in the proportion of GFP⁺ SVZ cells that were Tbr2⁺ (**Fig. 2D, E**), and (iv) in the proportion of GFP⁺ cells that were Tbr2⁺ and PH3⁺ and showed a basal location (**Fig. 2F**). In contrast, neither 11B lacking the mitochondrial targeting sequence (11B Δ 2-21) nor HA-tagged 11B (HA-11B) were able to cause an increase in mitotic and interphase BPs as compared to control (**Fig. 2A-F**). These results demonstrate that, using embryonic mouse neocortex as a test system, the mitochondrial localization of 11B is essential for its ability to increase BP, specifically Tbr2⁺ bIP, abundance.

20

11B physically interacts with ANT

We sought to elucidate the molecular mechanisms by which 11B, acting in mitochondria, increases BP abundance. To this end, we first performed pulldown assays from mouse E15.5

brain lysate using recombinant GST or GST-11B (**Figure 3A**), followed by mass spectrometry, in order to identify proteins interacting with 11B. This led to the identification of four membrane proteins that were specifically present in the GST-11B pulldown samples compared with the GST pulldown samples (**Figure 3B**). Three of these proteins reside in the inner mitochondrial membrane, namely adenine nucleotide translocase 2 (ANT2), phosphate carrier (PiC) and adenine nucleotide translocase 1 (ANT1). Importantly, other mitochondrial proteins of similar abundance as ANT were not found to be enriched in the GST-11B pulldown samples compared with the GST pulldown samples, indicating that the presence of ANT in the GST-11B pulldown samples reflected a specific interaction with 11B.

To determine whether the presence of ANT2, PiC and ANT1 in the GST-11B pulldown samples was due to an interaction (directly or indirectly) with the 11B truncated GAP domain or with the 11B-specific domain, we performed pulldown assays also with GST-11A220, which contains the truncated GAP domain but lacks the 11B-specific domain (**Figure 3A**). Mass spectrometry revealed that ANT2, PiC and ANT1 were also present in the GST-11A220 pulldown samples (**Figure 3B**), suggesting that the presence of ANT2, PiC and ANT1 in the pulldown samples was due to an interaction of at least one of these three mitochondrial membrane proteins with the truncated GAP domain rather than with the 11B-specific domain.

We next focused on ANT2 because it was the mitochondrial membrane protein most enriched in the GST-11B pulldown samples. Specifically, to corroborate the pulldown findings and to determine whether the presence of ANT2 in the pulldown samples reflected a direct physical interaction with 11B, we first performed immunoprecipitation of C-terminally HA-tagged 11B and C-terminally FLAG-tagged ANT2, both co-expressed in COS-7 cells, which are fibroblast-

like cells derived from the African green monkey. Immunoblot analyses showed that ANT2-FLAG was specifically co-immunoprecipitated with 11B-HA, and conversely 11B-HA was specifically co-immunoprecipitated with ANT2-FLAG (**Figure 3C**). Second, to demonstrate the direct physical interaction between 11B and ANT2, we performed *in vitro* binding assays of various mixtures of recombinant GST, GST-11B, maltose binding protein (MBP) and MBP-ANT2 (**Figure 3D top**) followed by GST pulldown. This revealed the specific presence of MBP-ANT2 in the GST-11B pulldown sample (**Figure 3D bottom**). Although the affinity of this interaction requires further investigation, these results, when taken together, indicate that 11B directly binds to ANT2 via its GAP domain, not only *in vitro* but also in living cells.

Expression of excess ANT in embryonic mouse neocortex blocks the ability of 11B to increase BPs

In light of these findings, we examined by IUE of E13.5 mouse neocortex whether expression of excess ANT2 would affect the ability of 11B to increase BP levels. Analysis at E14.5 showed that 11B more than doubled the level of mitotic BPs derived from targeted cells (GFP+) (**Figure 3E, F**), as observed previously (Florio et al., 2015; Florio et al., 2016). Remarkably, however, co-expression of ANT2 with 11B completely abrogated this effect of 11B, while expression of ANT2 alone (i.e. in the absence of 11B) had no effect on its own (**Figure 3E, F**). Thus, expression of ANT along with 11B in embryonic mouse neocortex blocks the ability of 11B to increase BPs. Because of the nature of IUE, it is difficult to estimate how much ANT2 relative to 11B is needed to block the effect of 11B.

11B delays the opening of the mitochondrial permeability transition pore (mPTP), a target of ANT function

Given the specific physical interaction of 11B with ANT2, we next explored whether 11B would affect ANT functions. There are two major functions of ANT, (i) the translocation of ADP/ATP across the inner mitochondrial membrane (Halestrap and Richardson, 2015), and (ii) the regulation of the mitochondrial permeability transition pore (mPTP, as shown for ANT1), which controls the concentration of small molecules in the mitochondrial matrix such as calcium (Doczi et al., 2016; Halestrap and Richardson, 2015). We first examined whether 11B affects the ADP/ATP translocation activity of ANT by measuring the mitochondrial membrane potential (**Figure 4A**) and the extra-mitochondrial ATP concentration (**Figure 4B**) in response to the addition of ADP and subsequently the dose-dependent effect of uncoupler SF6847, using permeabilized COS-7 cells that had been transfected with empty vector (control) or 11B-expressing plasmid. We did not detect any significant changes in the mitochondrial membrane potential (**Figure 4A**) and the extra-mitochondrial ATP concentration (**Figure 4B**) over time between control and 11B-transfected cells, suggesting that 11B does not affect the ADP/ATP translocation activity of ANT.

To examine whether 11B affects the second major ANT function, the regulation of the mPTP, we measured the swelling of mitochondria, an indicator of mPTP opening (Doczi et al., 2016; Halestrap and Richardson, 2015), in COS-7 cells transfected with an RFP targeted to mitochondria and either empty vector (control) or 11B-expressing plasmid. mPTP formation/opening was induced by calcimycin, a calcium ionophore, and mitochondrial swelling was measured by determining the so-called normalized thinness ratio (δTR) and the changes

induced in the δ TR upon mPTP opening (referred to as δ TR amplitude) (**Figure S3A**), a previously established method (Doczi et al., 2016). Compared to control, 11B-transfected COS-7 cells showed a significant delay in the onset of mPTP opening (**Figure 4C, Figure S3B**) and a significant decrease in the percentage of cells exhibiting mPTP opening (**Figure 4C**). In contrast, we did not observe any significant change in the δ TR amplitude between control and 11B-transfected COS-7 cells (**Figure S3C**). Hence, 11B specifically delays mPTP formation/opening.

Interference with mPTP opening and inhibition of the mPTP regulator ANT increases BP abundance

The cyclic peptide cyclosporine A (CsA) is known to inhibit mPTP opening (Halestrap and Richardson, 2015). If the delay in mPTP opening by 11B underlies its ability to increase BPs, and if mPTP regulation in general has a role in determining BP abundance, one might expect that inhibition of mPTP opening by CsA may also increase BP levels, even in the absence of 11B. We explored this possibility by subjecting E13.5 mouse neocortex for 24 h to HERO culture (Schenk et al., 2009) in the absence or presence of 4 μ M CsA. We first verified that under the present conditions, CsA would affect the activity of two target proteins known to be inhibited by CsA, peptidylprolylisomerase (PPIase) and the protein phosphatase calcineurin (Folda et al., 2016; Friberg et al., 1998). Indeed, treatment of embryonic mouse neocortex with CsA significantly reduced the activity of PPIase (**Figure S4A**) and calcineurin (**Figure S4B**). Importantly, CsA treatment resulted in a more than two-fold increase in the level of mitotic BPs (**Figure 4D, F**), without a significant increase in the level of mitotic APs (**Figure 4D, E**). Given that CsA also inhibited calcineurin, we in parallel examined the effects of the drug FK506, which is known to

inhibit calcineurin (Friberg et al., 1998), confirmed for the present conditions (**Figure S4B**), but does not affect the mPTP (Friberg et al., 1998). In contrast to CsA, FK506 treatment had no effect on mitotic BP abundance (**Figure 4D, F**). Taken together, these data indicate that inhibition of mPTP opening by CsA increases BP abundance.

5

In light of these data, and considering that the delay in mPTP opening by 11B (**Figure 4C, Figure S3B**) likely reflected its interaction with ANT (**Figure 3B**), we wondered whether inhibiting ANT function would have a similar effect on BP abundance as inhibiting mPTP opening by CsA. The bacteria-derived mitochondrial toxin bongkrekic acid (BKA) is a pan-ANT inhibitor (Halestrap and Brenner, 2003). We therefore examined the effects of BKA administered by injection into the lateral ventricles of E13.5 mouse embryos *in utero*. Analysis of the E14.5 neocortex revealed that BKA treatment doubled the level of mitotic BPs (**Figure 4G, I**) and significantly increased the abundance of cells expressing the BP marker Tbr2 (**Figure 4G, J**), but had no effect on mitotic AP abundance (**Figure 4G, H**). Hence, ANT inhibition (**Figure 4G-J**), like inhibition of mPTP opening (**Figure 4D-F**), increases BP abundance. Given that 11B specifically interacts with ANT (**Figure 3B-D**), this in turn suggests that the ability of 11B to increase BP abundance is based on its effect to delay mPTP opening, which likely involves an inhibition of the ANT function regulating the mPTP by 11B (**Figure 4C, Figure S3B**).

10

15

To examine whether the addition of mPTP- or ANT-inhibiting drugs would affect BP abundance in endogenously 11B-expressing fetal human neocortex, PCW11-14 human neocortical tissue was electroporated with GFP *ex vivo*, subjected to free-floating tissue (FFT) culture (Long et al., 2018) for 1 day, then incubated in FFT culture for another 2 days with CsA, FK506 or BKA, and analyzed. Neither treatment significantly increased the proportion of cycling (PCNA+) BPs

derived from targeted cells (GFP+) (**Figure S5**). This indicates that upon physiological 11B expression, which causes delayed mPTP opening via ANT inhibition, the addition of exogenous mPTP or ANT inhibitors does not result in a further increase in BP abundance.

5 **The delay of mPTP opening by 11B requires its human-specific C-terminal domain**

We next investigated which domain of 11B is responsible for the delay of mPTP opening. COS-7 cells transfected with 11A220 (see **Figure S1A**, however no HA-tag), in contrast to COS-7 cells transfected with 11B, did not show any delay in the onset of mPTP opening (**Figure 5A, Figure**
10 **S3B**). Moreover, 11A220-electroporated mouse neocortex did not show the increase in the abundance of mitotic BPs derived from targeted cells (GFP+) (**Figure 5B, C**). Together, these results indicate that the human-specific C-terminal domain of 11B (11B-specific domain) is essential for the 11B-induced delay of mPTP opening and the increase in BP abundance. This in turn implies that whereas the GAP domain of 11B, which is shared with 11A, mediates its
15 binding to ANT (**Figure 3A, B**), the 11B-specific domain mediates the inhibitory effect of 11B on the ANT function regulating the mPTP, and thereby the 11B-induced increase in BP abundance.

20 **11A220 acts in a dominant-negative manner on 11B's effects on delaying mPTP opening and increasing BPs**

The findings that 11A220 does not affect mPTP (**Figure 5A**) and BP abundance (**Figure 5B, C**) but is localized in mitochondria (**Figure S1D**) and interacts with ANT (**Figure 3B**) prompted us to analyze its potential dominant-negative action on 11B. Indeed, COS-7 cells co-transfected with

11B and 11A220, in contrast to COS-7 cells transfected with 11B alone, did not show any delay in the onset of mPTP opening (**Figure 5A, Figure S3B**). Moreover, mouse neocortex co-electroporated with 11B and 11A220 did not show the increase in the abundance of mitotic BPs derived from targeted cells (GFP+) typically observed upon eletroporation with 11B alone (**Figure 5B, C**). Together, these results indicate that 11A220 acts in a dominant-negative manner on the 11B-induced delay in the onset of mPTP opening and the increase in BP abundance.

11A220 decreases BP abundance in fetal human neocortex

The nucleotide sequence of the *11B* gene is essentially contained in that of the *11A* gene (Sudmant et al., 2010). It would therefore be rather difficult to obtain an *11B*-specific gene disruption or knock-down (using CRISPR/Cas9 or RNA interference, respectively) to examine the physiological role of 11B in fetal human neocortex. However, the dominant-negative action of 11A220 on the effects of exogenous 11B expressed in COS-7 cells (**Figure 5A**) and embryonic mouse neocortex (**Figure 5B, C**) provided us with the opportunity to explore a potential dominant-negative action of 11A220 on the effects of the endogenous, physiologically acting 11B in fetal human neocortex. To this end, we electroporated 11A220 into PCW11-14 human neocortical tissue *ex vivo*. Analysis after 3 days of FFT culture revealed that 11A220 significantly reduced the proportion of cycling (PCNA+) BPs derived from targeted cells (GFP+) (**Figure 5D-F**). Importantly, there was no change in this proportion between control and 11A220-electroporated embryonic mouse neocortex (**Figure 5B, C**), indicating that 11A220 does not have any negative effects on BP abundance in the absence of 11B. Hence, these data provide strong support for the notion that 11B, which is physiologically expressed in fetal human neocortex

(Florio et al., 2015; Florio et al., 2018) (**Figure 1I, Figure S2C, D**), indeed plays a major role in determining the abundance of BPs in fetal human neocortex.

Use of glutamine is essential for the 11B-induced increase in mitotic BP levels

5

How does the inhibitory effect on mPTP caused by 11B lead to the increase in mitotic BP levels?

We sought to obtain insight into this issue by examining metabolic pathways that are linked to mitochondrial function, (i) glycolysis, which under aerobic conditions fuels the TCA cycle, and (ii) glutaminolysis, i.e. the conversion of glutamine to glutamate which then also can fuel the

10

TCA cycle (Yang et al., 2017). To examine a potential role of glycolysis in the 11B-induced increase in mitotic BP levels, we used the glycolysis inhibitor 2-deoxyglucose (Wick et al., 1957).

Specifically, we electroporated mouse neocortex at E13.5 with EGFP together with either empty vector (control) or 11B. Twelve hours after IUE, the cerebral hemispheres dissected from the embryos were subjected to HERO culture for 12 h in the absence or presence of 0.5-5 mM 2-deoxyglucose. This 2-deoxyglucose treatment did not significantly reduce the 11B-induced increase in the proportion of mitotic BPs derived from targeted (GFP+) cells (**Figure 6A, B**).

15

To obtain a first indication for a possible role of glutaminolysis in the 11B-induced increase in mitotic BP levels, we followed the same protocol, incubating the mouse cerebral hemispheres in

20

HERO culture for 12 h, however, in the absence or presence of either 10 μ M 6-diazo-5-oxo-L-norleucine (DON) or 10 μ M bis-2-(5-phenylacetamido-1,3,4-thiadiazol-2-yl) ethyl sulfide (BPTES). DON is a glutamine antagonist that inhibits glutamine metabolism including the conversion of glutamine to glutamate (Pinkus, 1977; Vanhove et al., 2019), whereas BPTES is an inhibitor of glutaminase, preferentially of cytosolic glutaminase, and therefore acts more

specifically to inhibit glutamine-to-glutamate conversion (Robinson et al., 2007; Vanhove et al., 2019). Both the present DON treatment and BPTES treatment completely suppressed the 11B-induced increase in mitotic BP levels but had no effect on the mitotic BP levels observed upon control IUE (**Figure 6A, B**). These results show that glutamine-to-glutamate conversion is essential for the ability of 11B to increase mitotic BP levels.

To examine the relevance of these findings obtained with embryonic mouse neocortex for BP abundance in fetal human neocortex, PCW11-14 human neocortical tissue was electroporated with GFP *ex vivo*, subjected to FFT culture for 1 day, then incubated in FFT culture for another 2 days with 2-DG, DON or BPTES, and analyzed. DON and BPTES, but not 2-DG, significantly reduced the proportion of cycling (PCNA+) BPs derived from targeted cells (GFP+) (**Figure 6C, D**), indicating that glutaminolysis rather than glycolysis is required to maintain BP abundance in fetal human neocortex.

The requirement of glutamine-to-glutamate conversion for the 11B-induced BP expansion reflects an essential role of glutaminolysis

If the requirement of glutamine-to-glutamate conversion for the increase in mitotic BP levels by 11B reflects an essential role of glutaminolysis, that is, the import of glutamate into the mitochondrial matrix and its conversion to α -ketoglutarate to fuel the TCA cycle (Vanhove et al., 2019; Yang et al., 2017), one would expect a glutamine-dependent increase in mitochondrial respiration upon 11B expression. We therefore transfected COS-7 cells with empty vector (control) or 11B-expressing plasmid and measured the mitochondrial oxygen consumption rate

(OCR) in the absence and presence of glutamine. Whereas glutamine addition to control cells resulted in only a small increase in the mitochondrial OCR relative to the basal mitochondrial OCR measured without any substrate addition, glutamine addition to 11B-expressing cells led to a significant increase in the mitochondrial OCR (**Figure 6E**). This indicated that 11B expression caused a glutamine-dependent increase in mitochondrial respiration.

This conclusion was further corroborated by the results of measuring the maximal mitochondrial OCR of control and 11B-transfected COS-7 cells in the presence of the uncoupler DNP. Addition of glutamine to 11B-expressing cells resulted in a three-fold increase in the maximal OCR that was significantly greater than the increase in the maximal OCR upon glutamine addition to control cells (**Figure 6F**). We conclude that the requirement of glutamine-to-glutamate conversion for the increase in mitotic BP levels by 11B (**Figure 6A-D**), together with the glutamine-dependent increase in mitochondrial respiration upon 11B expression (**Figure 6E, F**), reflects an essential role of glutaminolysis for the BP expansion by 11B.

11B increases mitochondrial calcium concentration, a parameter promoting glutaminolysis

We sought to provide a link between the 11B-induced delay in mPTP opening and the dependence of the 11B-induced BP expansion on glutaminolysis. To this end, we explored whether 11B expression would increase calcium levels in the mitochondrial matrix, a known consequence of inhibiting mPTP (Brookes et al., 2004; De Marchi et al., 2014). An increase in mitochondrial calcium levels appeared to be an attractive candidate, as mitochondrial dehydrogenases are known to be critical for glutaminolysis and activated by increasing mitochondrial calcium levels (Cannino et al., 2018; Lawlis and Roche, 1981; Rutter and Denton,

1989). We therefore transfected COS-7 cells with empty vector (control) or 11B-expressing plasmid, together with the FRET-based calcium indicator 4mtD3cpV (Palmer and Tsien, 2006). Upon 11B expression, mitochondria indeed showed a small, but significant, increase in the basal mitochondrial calcium concentration (**Figure 6A**).

5

Next, we applied extracellular ATP to elevate cytosolic calcium levels, which is known to result in increased mitochondrial calcium uptake ζ refs. Under these conditions, the mitochondrial calcium level was indeed increased, but significantly more so upon 11B expression than control (**Figure 6A**). These data suggest that the 11B-induced delay in mPTP opening results in increased mitochondrial calcium levels. This in turn would promote glutaminolysis, thus providing a link between the effects of 11B on mPTP and the 11B-induced, glutaminolysis-dependent BP expansion.

10

Discussion

The present study advances our understanding of the molecular basis underlying the evolutionary expansion of the human neocortex in four major ways. First, by exploiting our finding that 11A220 is a dominant-negative inhibitor of the effects of 11B, we demonstrate that 11B is required to maintain the physiological BP level in the fetal human neocortex (**Figure 5F**). This constitutes the first evidence for a biological role of 11B in human BP abundance.

Second, in contrast to the 11A protein, which is found in the nucleoplasm, the 11B protein exhibits a strikingly different subcellular localization, being found in mitochondria. This difference in subcellular localization reflects the loss of nuclear localization signals from the 11B protein that are present in the ancestral, much longer 11A protein. This loss, in turn, functionally unmasks an N-terminal mitochondrial import sequence that is present in both 11A and 11B (**Figure 7B**). Of note, the ancestral 11B protein, that is, the 11B protein originally encoded by the *11B* gene prior to the occurrence of the C→G single nucleotide substitution that gave rise to the modern 11B protein (Florio et al., 2016), still contains one of the nuclear localization signals and accordingly is found in the nucleoplasm rather than in mitochondria. Hence, the C→G single nucleotide substitution changed two principal features of 11B, (i) its subcellular localization, resulting in its import into mitochondria, (ii) its C-terminal protein sequence, resulting in the loss of Rho-GAP activity (Florio et al., 2015; Florio et al., 2016) and the generation of the 11B-specific domain that is essential for its action in mitochondria (**Figure 7B**). Together, these two features endow modern 11B (as compared to ancestral 11B) with a new function that enables this protein to increase BP abundance.

Third, the mitochondrial localization of 11B is necessary for its function to increase BP abundance. As to its mechanism of action within mitochondria, 11B physically interacts with the adenine nucleotide translocase ANT, a regulator of the mPTP (**Figure 7B**). Our data showing that (i) 11B causes a delay in the opening of the mPTP, and (ii) both pharmacological inhibition of ANT and interference with mPTP opening increase BP abundance, collectively indicate that ANT-mediated negative regulation of mPTP opening has a key role in the 11B-induced increase in BP abundance (**Figure 7C**). Our data are consistent with (i) observations obtained in mouse neurospheres showing that pharmacological inhibition of mPTP increases their proliferation (Hou et al., 2012), (ii) the finding that KO mice for cyclophilin D, a positive regulator of mPTP, show increased proliferation of embryonic fibroblasts and T-cells (Tavecchio et al., 2013; Tzelepis et al., 2018), and (iii) the report that an ANT knockdown results in stimulated proliferation of H9c2 cardiomyoblasts (R et al., 2019). Moreover, mPTP inhibition is a typical feature of tumor cells (Bernardi et al., 2015). Remarkably, whereas the interaction with ANT occurs via 11B's truncated GAP domain that is shared with 11A, the negative regulation of mPTP opening requires the 11B-specific C-terminal domain of 11B.

Forth, the consequences of the negative regulation of mPTP opening by 11B for mitochondrial metabolism are remarkable. A delay in the onset of mPTP opening is known to lead to a higher mitochondrial calcium concentration (Bernardi et al., 2015; Halestrap and Richardson, 2015). This in turn will affect various aspects of mitochondrial metabolism (Cannino et al., 2018; Gardner et al., 1995; Llorente-Folch et al., 2015; Tretter and Adam-Vizi, 2000; Vizan et al., 2008), notably key enzymes of the TCA cycle. Specifically, an increased mitochondrial calcium concentration is known to activate α -ketoglutarate dehydrogenase, the enzyme catalyzing the

conversion of α -ketoglutarate to succinyl-CoA (Cannino et al., 2018; Lawlis and Roche, 1981; Rutter and Denton, 1989) (**Figure 7C**). Hence, the increased mitochondrial calcium concentration upon mPTP inhibition would favor fueling the TCA cycle by glutaminolysis (Cannino et al., 2018; Tretter and Adam-Vizi, 2000; Vanhove et al., 2019; Yang et al., 2017).

5 Consistent with these considerations, we indeed observed – together with a delayed mPTP opening – an increased mitochondrial calcium concentration upon 11B expression (**Figure 7A**), as well as an increase in glutamine-dependent mitochondrial respiration (**Figure 6E, F**). Taken together, these data provide a mechanistic explanation why the glutamine-to-glutamate conversion in the cytosol is essential for the ability of 11B to increase BP abundance (**Figure**
10 **7C**).

Importantly, an increase in glutaminolysis is known to be a hallmark of highly mitotically active cells, notably tumor cells (Yang et al., 2017), and glutaminolysis has been shown to causally contribute to cell proliferation (Chinopoulos and Seyfried, 2018; Yang et al., 2017). The present
15 demonstration that increasing glutaminolysis is essential for the ability of 11B to increase BP abundance is consistent with previous studies showing that mouse fibroblasts show elevated glutaminolysis upon mPTP inhibition (Tavecchio et al., 2015) and that glutaminolysis is essential for cell cycle progression (Colombo et al., 2011). On a more general note, the present data on the human-specific gene *I1B* add a new facet to the notion that mitochondrial dynamics and
20 metabolism can exert key roles in neural stem cell proliferation vs. differentiation (Beckervordersandforth et al., 2017; Khacho et al., 2016; Knobloch and Jessberger, 2017; Zheng et al., 2016). Specifically, the mitochondria-based metabolic changes in BPs that evolved as a consequence of the single C→G nucleotide substitution in the *I1B* gene provide novel insight

how the increase in BP abundance and proliferation led to the evolutionary expansion of the human neocortex.

References

- Akerman, K.E., and Wikstrom, M.K. (1976). Safranin as a probe of the mitochondrial membrane potential. *FEBS letters* 68, 191-197.
- 5 Antonacci, F., Dennis, M.Y., Huddleston, J., Sudmant, P.H., Steinberg, K.M., Rosenfeld, J.A., Miroballo, M., Graves, T.A., Vives, L., Malig, M., *et al.* (2014). Palindromic GOLGA8 core duplicons promote chromosome 15q13.3 microdeletion and evolutionary instability. *Nat Genet* 46, 1293-1302.
- 10 Beckervordersandforth, R., Ebert, B., Schaffner, I., Moss, J., Fiebig, C., Shin, J., Moore, D.L., Ghosh, L., Trincherro, M.F., Stockburger, C., *et al.* (2017). Role of mitochondrial metabolism in the control of early lineage progression and aging phenotypes in adult hippocampal Neurogenesis. *Neuron* 93, 560-573 e566.
- 15 Bernardi, P., Rasola, A., Forte, M., and Lippe, G. (2015). The mitochondrial permeability transition pore: channel formation by F-ATP synthase, integration in signal transduction, and role in pathophysiology. *Physiol Rev* 95, 1111-1155.
- Brookes, P.S., Yoon, Y., Robotham, J.L., Anders, M.W., and Sheu, S.S. (2004). Calcium, ATP, and ROS: a mitochondrial love-hate triangle. *American journal of physiology Cell physiology* 287, C817-833.
- 20 Cannino, G., Ciscato, F., Masgras, I., Sanchez-Martin, C., and Rasola, A. (2018). Metabolic plasticity of tumor cell mitochondria. *Front Oncol* 8, 333.
- Chinopoulos, C., and Seyfried, T.N. (2018). Mitochondrial substrate-level phosphorylation as energy source for glioblastoma: review and hypothesis. *ASN Neuro* 10, 1-27.
- Chinopoulos, C., Vajda, S., Csanady, L., Mandi, M., Mathe, K., and Adam-Vizi, V. (2009). A novel kinetic assay of mitochondrial ATP-ADP exchange rate mediated by the ANT. *Biophys J* 25 96, 2490-2504.
- Colombo, S.L., Palacios-Callender, M., Frakich, N., Carcamo, S., Kovacs, I., Tudzarova, S., and Moncada, S. (2011). Molecular basis for the differential use of glucose and glutamine in cell proliferation as revealed by synchronized HeLa cells. *Proc Natl Acad Sci U S A* 108, 21069-21074.
- 30 De Marchi, E., Bonora, M., Giorgi, C., and Pinton, P. (2014). The mitochondrial permeability transition pore is a dispensable element for mitochondrial calcium efflux. *Cell calcium* 56, 1-13.
- Dehay, C., Kennedy, H., and Kosik, K.S. (2015). The outer subventricular zone and primate-specific cortical complexification. *Neuron* 85, 683-694.
- 35 Doczi, J., Torocsik, B., Echaniz-Laguna, A., Mousson de Camaret, B., Starkov, A., Starkova, N., Gal, A., Molnar, M.J., Kawamata, H., Manfredi, G., *et al.* (2016). Alterations in voltage-sensing of the mitochondrial permeability transition pore in ANT1-deficient cells. *Scientific reports* 6, 26700.

- Dougherty, M.L., Underwood, J.G., Nelson, B.J., Tseng, E., Munson, K.M., Penn, O., Nowakowski, T.J., Pollen, A.A., and Eichler, E.E. (2018). Transcriptional fates of human-specific segmental duplications in brain. *Genome research* 28, 1566-1576.
- Englund, C., Fink, A., Lau, C., Pham, D., Daza, R.A., Bulfone, A., Kowalczyk, T., and Hevner, R.F. (2005). Pax6, Tbr2, and Tbr1 are expressed sequentially by radial glia, intermediate progenitor cells, and postmitotic neurons in developing neocortex. *The Journal of neuroscience : the official journal of the Society for Neuroscience* 25, 247-251.
- Fernandez, V., Llinares-Benadero, C., and Borrell, V. (2016). Cerebral cortex expansion and folding: what have we learned? *EMBO J* 35, 1021-1044.
- Fiddes, I.T., Lodewijk, G.A., Mooring, M., Bosworth, C.M., Ewing, A.D., Mantalas, G.L., Novak, A.M., van den Bout, A., Bishara, A., Rosenkrantz, J.L., *et al.* (2018). Human-specific NOTCH2NL genes affect notch signaling and cortical neurogenesis. *Cell* 173, 1356-1369 e1322.
- Fietz, S.A., and Huttner, W.B. (2011). Cortical progenitor expansion, self-renewal and neurogenesis-a polarized perspective. *Curr Opin Neurobiol* 21, 23-35.
- Florio, M., Albert, M., Taverna, E., Namba, T., Brandl, H., Lewitus, E., Haffner, C., Sykes, A., Wong, F.K., Peters, J., *et al.* (2015). Human-specific gene ARHGAP11B promotes basal progenitor amplification and neocortex expansion. *Science* 347, 1465-1470.
- Florio, M., Heide, M., Pinson, A., Brandl, H., Albert, M., Winkler, S., Wimberger, P., Huttner, W.B., and Hiller, M. (2018). Evolution and cell-type specificity of human-specific genes preferentially expressed in progenitors of fetal neocortex. *eLife* 7, e32332.
- Florio, M., Namba, T., Pääbo, S., Hiller, M., and Huttner, W.B. (2016). A single splice site mutation in human-specific *ARHGAP11B* causes basal progenitor amplification. *Science Advances* 2.
- Folda, A., Citta, A., Scalcon, V., Cali, T., Zonta, F., Scutari, G., Bindoli, A., and Rigobello, M.P. (2016). Mitochondrial Thioredoxin System as a Modulator of Cyclophilin D Redox State. *Sci Rep* 6, 23071.
- Friberg, H., Ferrand-Drake, M., Bengtsson, F., Halestrap, A.P., and Wieloch, T. (1998). Cyclosporin A, but not FK 506, protects mitochondria and neurons against hypoglycemic damage and implicates the mitochondrial permeability transition in cell death. *The Journal of neuroscience : the official journal of the Society for Neuroscience* 18, 5151-5159.
- Gardner, P.R., Raineri, I., Epstein, L.B., and White, C.W. (1995). Superoxide radical and iron modulate aconitase activity in mammalian cells. *The Journal of biological chemistry* 270, 13399-13405.
- Gerencser, A.A., Doczi, J., Torocsik, B., Bossy-Wetzler, E., and Adam-Vizi, V. (2008). Mitochondrial swelling measurement in situ by optimized spatial filtering: astrocyte-neuron differences. *Biophys J* 95, 2583-2598.
- Halestrap, A.P., and Brenner, C. (2003). The adenine nucleotide translocase: a central component of the mitochondrial permeability transition pore and key player in cell death. *Curr Med Chem* 10, 1507-1525.

- Halestrap, A.P., and Richardson, A.P. (2015). The mitochondrial permeability transition: a current perspective on its identity and role in ischaemia/reperfusion injury. *J Mol Cell Cardiol* 78, 129-141.
- 5 He, W., Bai, G., Zhou, H., Wei, N., White, N.M., Lauer, J., Liu, H., Shi, Y., Dumitru, C.D., Lettieri, K., *et al.* (2015). CMT2D neuropathy is linked to the neomorphic binding activity of glycyl-tRNA synthetase. *Nature* 526, 710-714.
- Hou, Y., Ouyang, X., Wan, R., Cheng, H., Mattson, M.P., and Cheng, A. (2012). Mitochondrial superoxide production negatively regulates neural progenitor proliferation and cerebral cortical development. *Stem Cells* 30, 2535-2547.
- 10 Johnson, M.B., Wang, P.P., Atabay, K.D., Murphy, E.A., Doan, R.N., Hecht, J.L., and Walsh, C.A. (2015). Single-cell analysis reveals transcriptional heterogeneity of neural progenitors in human cortex. *Nat Neurosci* 18, 637-646.
- Kagawa, Y., Matsumoto, S., Kamioka, Y., Mimori, K., Naito, Y., Ishii, T., Okuzaki, D., Nishida, N., Maeda, S., Naito, A., *et al.* (2013). Cell cycle-dependent Rho GTPase activity dynamically regulates cancer cell motility and invasion in vivo. *PLoS One* 8, e83629.
- 15 Kalebic, N., Gilardi, C., Albert, M., Namba, T., Long, K.R., Kostic, M., Langen, B., and Huttner, W.B. (2018). Human-specific ARHGAP11B induces hallmarks of neocortical expansion in developing ferret neocortex. *eLife* 7.
- Kalebic, N., Gilardi, C., Stepien, B., Wilsch-Brauninger, M., Long, K.R., Namba, T., Florio, M., Langen, B., Lombardot, B., Shevchenko, A., *et al.* (2019). Neocortical expansion due to increased proliferation of basal progenitors is linked to changes in their morphology. *Cell Stem Cell* 24, 535-550 e539.
- 20 Kawamata, H., Starkov, A.A., Manfredi, G., and Chinopoulos, C. (2010). A kinetic assay of mitochondrial ADP-ATP exchange rate in permeabilized cells. *Anal Biochem* 407, 52-57.
- 25 Khacho, M., Clark, A., Svoboda, D.S., Azzi, J., MacLaurin, J.G., Meghaizel, C., Sesaki, H., Lagace, D.C., Germain, M., Harper, M.E., *et al.* (2016). Mitochondrial dynamics impacts stem cell identity and fate decisions by regulating a nuclear transcriptional program. *Cell Stem Cell* 19, 232-247.
- Knobloch, M., and Jessberger, S. (2017). Metabolism and neurogenesis. *Curr Opin Neurobiol* 42, 45-52.
- 30 Lawlis, V.B., and Roche, T.E. (1981). Regulation of bovine kidney alpha-ketoglutarate dehydrogenase complex by calcium ion and adenine nucleotides. Effects on S0.5 for alpha-ketoglutarate. *Biochemistry* 20, 2512-2518.
- Llorente-Folch, I., Rueda, C.B., Pardo, B., Szabadkai, G., Duchen, M.R., and Satrustegui, J. 35 (2015). The regulation of neuronal mitochondrial metabolism by calcium. *J Physiol* 593, 3447-3462.
- Long, K.R., Newland, B., Florio, M., Kalebic, N., Langen, B., Kolterer, A., Wimberger, P., and Huttner, W.B. (2018). Extracellular matrix components HAPLN1, Lumican, and Collagen I 40 cause hyaluronic acid-dependent folding of the developing human neocortex. *Neuron* 99, 702-719.

- Lui, J.H., Hansen, D.V., and Kriegstein, A.R. (2011). Development and evolution of the human neocortex. *Cell* 146, 18-36.
- 5 Mayne, L., Kan, Z.Y., Chetty, P.S., Ricciuti, A., Walters, B.T., and Englander, S.W. (2011). Many overlapping peptides for protein hydrogen exchange experiments by the fragment separation-mass spectrometry method. *J Am Soc Mass Spectrom* 22, 1898-1905.
- Mehta, S., Aye-Han, N.N., Ganesan, A., Oldach, L., Gorshkov, K., and Zhang, J. (2014). Calmodulin-controlled spatial decoding of oscillatory Ca²⁺ signals by calcineurin. *eLife* 3, e03765.
- 10 Meyer, M., Kircher, M., Gansauge, M.T., Li, H., Racimo, F., Mallick, S., Schraiber, J.G., Jay, F., Prufer, K., de Filippo, C., *et al.* (2012). A high-coverage genome sequence from an archaic Denisovan individual. *Science* 338, 222-226.
- Mokranjac, D., and Neupert, W. (2009). Thirty years of protein translocation into mitochondria: unexpectedly complex and still puzzling. *Biochim Biophys Acta* 1793, 33-41.
- 15 Namba, T., and Huttner, W.B. (2017). Neural progenitor cells and their role in the development and evolutionary expansion of the neocortex. *WIREs Dev Biol* 6, e256.
- Namba, T., Kibe, Y., Funahashi, Y., Nakamuta, S., Takano, T., Ueno, T., Shimada, A., Kozawa, S., Okamoto, M., Shimoda, Y., *et al.* (2014). Pioneering axons regulate neuronal polarization in the developing cerebral cortex. *Neuron* 81, 814-829.
- 20 Nemeth, B., Doczi, J., Csete, D., Kacso, G., Ravasz, D., Adams, D., Kiss, G., Nagy, A.M., Horvath, G., Tretter, L., *et al.* (2016). Abolition of mitochondrial substrate-level phosphorylation by itaconic acid produced by LPS-induced Irg1 expression in cells of murine macrophage lineage. *FASEB J* 30, 286-300.
- Palmer, A.E., and Tsien, R.Y. (2006). Measuring calcium signaling using genetically targetable fluorescent indicators. *Nat Protoc* 1, 1057-1065.
- 25 Paridaen, J.T., Huttner, W.B., and Wilsch-Brauninger, M. (2015). Analysis of primary cilia in the developing mouse brain. *Methods Cell Biol* 127, 93-129.
- Pascal, B.D., Willis, S., Lauer, J.L., Landgraf, R.R., West, G.M., Marciano, D., Novick, S., Goswami, D., Chalmers, M.J., and Griffin, P.R. (2012). HDX workbench: software for the analysis of H/D exchange MS data. *J Am Soc Mass Spectrom* 23, 1512-1521.
- 30 Pinkus, L.M. (1977). Glutamine binding sites. *Methods in enzymology* 46, 414-427.
- Pollen, A.A., Nowakowski, T.J., Chen, J., Retallack, H., Sandoval-Espinosa, C., Nicholas, C.R., Shuga, J., Liu, S.J., Oldham, M.C., Diaz, A., *et al.* (2015). Molecular identity of human outer radial glia during cortical development. *Cell* 163, 55-67.
- 35 Prüfer, K., Racimo, F., Patterson, N., Jay, F., Sankararaman, S., Sawyer, S., Heinze, A., Renaud, G., Sudmant, P.H., de Filippo, C., *et al.* (2014). The complete genome sequence of a Neanderthal from the Altai Mountains. *Nature* 505, 43-49.
- R, M.P.-R., Chapa-Dubocq, X., Guzman-Hernandez, R., Jang, S., C, A.T.-R., Ayala-Pena, S., and Javadov, S. (2019). The Role of Adenine Nucleotide Translocase in the Assembly of Respiratory Supercomplexes in Cardiac Cells. *Cells* 8.

- Rakic, P. (2009). Evolution of the neocortex: a perspective from developmental biology. *Nat Rev Neurosci* 10, 724-735.
- Robinson, M.M., McBryant, S.J., Tsukamoto, T., Rojas, C., Ferraris, D.V., Hamilton, S.K., Hansen, J.C., and Curthoys, N.P. (2007). Novel mechanism of inhibition of rat kidney-type glutaminase by bis-2-(5-phenylacetamido-1,2,4-thiadiazol-2-yl)ethyl sulfide (BPTES). *The Biochemical journal* 406, 407-414.
- Rutter, G.A., and Denton, R.M. (1989). The binding of Ca²⁺ ions to pig heart NAD⁺-isocitrate dehydrogenase and the 2-oxoglutarate dehydrogenase complex. *The Biochemical journal* 263, 453-462.
- Schenk, J., Wilsch-Brauninger, M., Calegari, F., and Huttner, W.B. (2009). Myosin II is required for interkinetic nuclear migration of neural progenitors. *Proc Natl Acad Sci U S A* 106, 16487-16492.
- Sudmant, P.H., Kitzman, J.O., Antonacci, F., Alkan, C., Malig, M., Tsalenko, A., Sampas, N., Bruhn, L., Shendure, J., and Eichler, E.E. (2010). Diversity of human copy number variation and multicopy genes. *Science* 330, 641-646.
- Sun, T., and Hevner, R.F. (2014). Growth and folding of the mammalian cerebral cortex: from molecules to malformations. *Nat Rev Neurosci* 15, 217-232.
- Suzuki, I.K., Gacquer, D., Van Heurck, R., Kumar, D., Wojno, M., Bilheu, A., Herpoel, A., Lambert, N., Cheron, J., Polleux, F., *et al.* (2018). Human-specific NOTCH2NL genes expand cortical neurogenesis through Delta/Notch regulation. *Cell* 173, 1370-1384 e1316.
- Tavecchio, M., Lisanti, S., Bennett, M.J., Languino, L.R., and Altieri, D.C. (2015). Deletion of Cyclophilin D impairs beta-oxidation and promotes glucose metabolism. *Scientific reports* 5, 15981.
- Tavecchio, M., Lisanti, S., Lam, A., Ghosh, J.C., Martin, N.M., O'Connell, M., Weeraratna, A.T., Kossenkov, A.V., Showe, L.C., and Altieri, D.C. (2013). Cyclophilin D extramitochondrial signaling controls cell cycle progression and chemokine-directed cell motility. *The Journal of biological chemistry* 288, 5553-5561.
- Tretter, L., and Adam-Vizi, V. (2000). Inhibition of Krebs cycle enzymes by hydrogen peroxide: A key role of [alpha]-ketoglutarate dehydrogenase in limiting NADH production under oxidative stress. *J Neurosci* 20, 8972-8979.
- Tzelepis, F., Blagih, J., Khan, N., Gillard, J., Mendonca, L., Roy, D.G., Ma, E.H., Joubert, P., Jones, R.G., and Divangahi, M. (2018). Mitochondrial cyclophilin D regulates T cell metabolic responses and disease tolerance to tuberculosis. *Science immunology* 3.
- Vaid, S., Camp, J.G., Hersemann, L., Eugster Oegema, C., Heninger, A.K., Winkler, S., Brandl, H., Sarov, M., Treutlein, B., Huttner, W.B., *et al.* (2018). A novel population of Hopx-dependent basal radial glial cells in the developing mouse neocortex. *Development* 145.
- Vanhove, K., Derveaux, E., Graulus, G.J., Mesotten, L., Thomeer, M., Noben, J.P., Guedens, W., and Adriaensens, P. (2019). Glutamine Addiction and Therapeutic Strategies in Lung Cancer. *International journal of molecular sciences* 20.
- Vizan, P., Mazurek, S., and Cascante, M. (2008). Robust metabolic adaptation underlying tumor progression. *Metabolomics* 4, 1-12.

- Walters, B.T., Ricciuti, A., Mayne, L., and Englander, S.W. (2012). Minimizing back exchange in the hydrogen exchange-mass spectrometry experiment. *J Am Soc Mass Spectrom* 23, 2132-2139.
- 5 Wick, A.N., Drury, D.R., Nakada, H.I., and Wolfe, J.B. (1957). Localization of the primary metabolic block produced by 2-deoxyglucose. *The Journal of biological chemistry* 224, 963-969.
- Wiedemann, N., and Pfanner, N. (2017). Mitochondrial machineries for protein import and assembly. *Annu Rev Biochem* 86, 685-714.
- Yang, L., Venneti, S., and Nagrath, D. (2017). Glutaminolysis: a hallmark of cancer metabolism. *Annu Rev Biomed Eng* 19, 163-194.
- 10 Yung, Y.C., Mutoh, T., Lin, M.E., Noguchi, K., Rivera, R.R., Choi, J.W., Kingsbury, M.A., and Chun, J. (2011). Lysophosphatidic acid signaling may initiate fetal hydrocephalus. *Sci Transl Med* 3, 99ra87.
- Zanin, E., Desai, A., Poser, I., Toyoda, Y., Andree, C., Moebius, C., Bickle, M., Conradt, B., Piekny, A., and Oegema, K. (2013). A conserved RhoGAP limits M phase contractility and coordinates with microtubule asters to confine RhoA during cytokinesis. *Dev Cell* 26, 496-510.
- 15 Zhang, Y. (2008). I-TASSER server for protein 3D structure prediction. *BMC bioinformatics* 9, 40.
- Zheng, X., Boyer, L., Jin, M., Mertens, J., Kim, Y., Ma, L., Hamm, M., Gage, F.H., and Hunter, T. (2016). Metabolic reprogramming during neuronal differentiation from aerobic glycolysis to neuronal oxidative phosphorylation. *eLife* 5.
- 20

Acknowledgments: We are grateful to the late W. Neupert for useful discussions, and thank the Services and Facilities of the Max Planck Institute of Molecular Cell Biology and Genetics for

25 their technical support, notably J. Helppi and his team of the Biomedical Services (BMS), J. Peychl and his team of the Light Microscopy Facility, the team of the Antibody Facility, and the team of the Mass Spectrometry Facility. We thank D. Gerrelli, S. Lisgo and their teams at the HDBR for the invaluable support from this resource, as well as K. Kaibuchi for kindly providing pCAGGS-HA-C and pCAGGS-HA-N-kk1 plasmids and R. Hevner for kindly providing anti-

30 Tbr2 antibody. T.N. was supported by a long-term fellowship from the Yamada Science Foundation. **Funding:** C.C. was supported by NKFIH (Nemzeti Kutatási, Fejlesztési és Innovációs Hivatal) KH129567. W.B.H. was supported by grants from the DFG (SFB 655, A2),

the ERC (250197) and ERA-NET NEURON (MicroKin). **Author contributions:**

Conceptualization: T.N., W.B.H.; Formal analysis: T.N., J.D., N.K., J.L., C.C.; Investigation:

T.N., J.D., A.P., L.X., N.K., M.W.-B., K.L., S.V., J.L., A.S., C.C.; Resources: A.B., B.B., P.K.,

D.D., P.W.; Visualization: T.N.; Writing – original draft: T.N., with input from J.L., T.K. and

5 C.C.; Writing – review & editing: T.N., W.B.H.; Funding acquisition: C.C., W.B.H.; Project

administration and Supervision: W.B.H. **Declaration of Interests:** The authors declare no

competing interests.

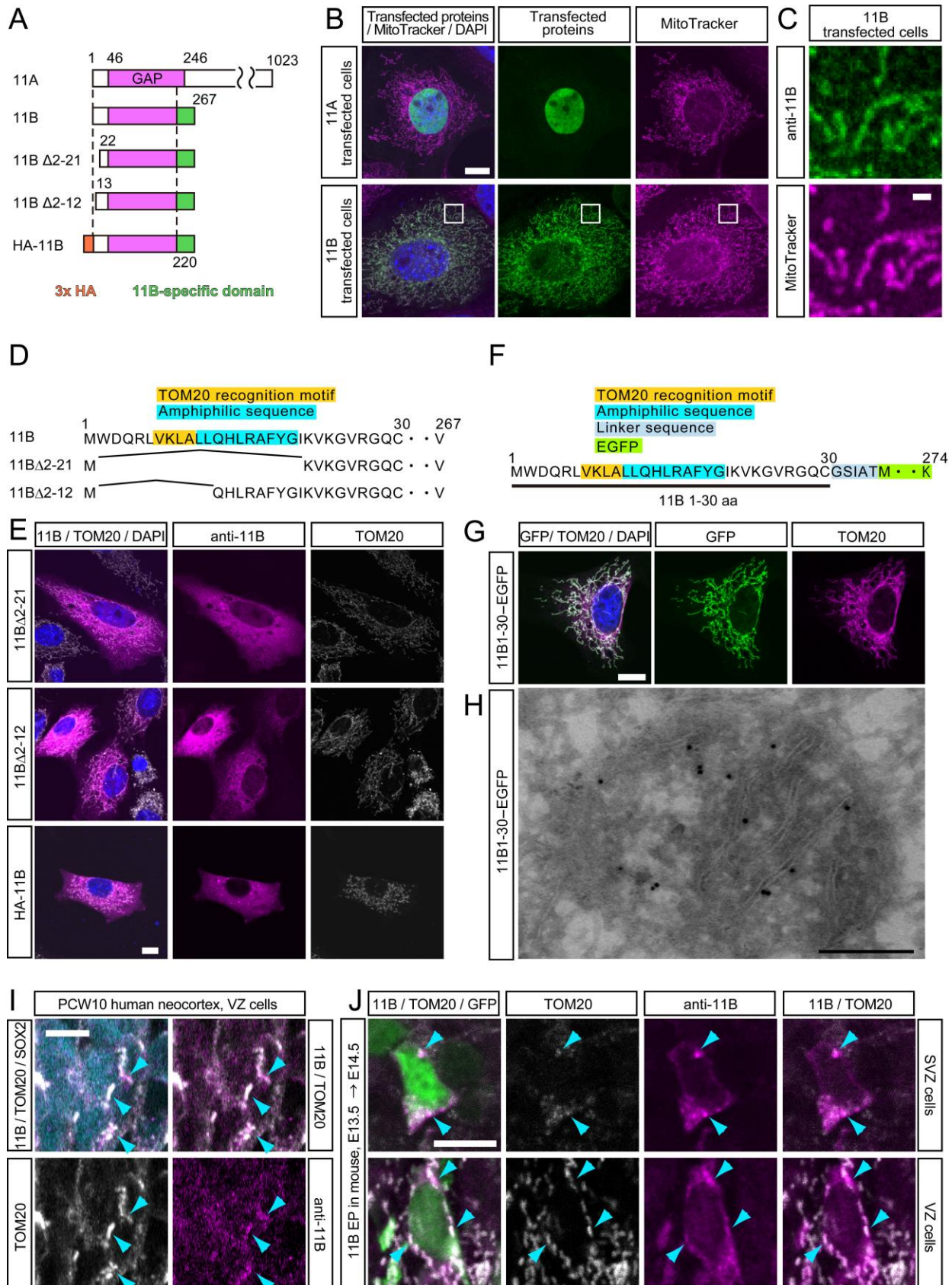


Figure 1. 11B is localized in mitochondria.

(A) Domain structure of wt 11A and of wt 11B and its indicated mutants. Magenta, GAP domain; orange, 3x HA-tag; green, 11B-specific domain comprising the 47 amino acid human-specific C-terminal sequence. Numbers indicate the initiator methionine (1, left vertical dashed line), the beginning (46) and end (246) of the GAP domain, the C-terminal amino acid of 11A (1023) and 11B (267), and the N-terminal amino acid of 11B Δ 2-21 (22) and 11B Δ 2-12 (13); the right vertical dashed line indicates amino acid residue 220.

(B, C) NIH-3T3 cells were transfected with 11A or 11B, followed 24 h later by 11A (top row) and 11B (bottom row) immunofluorescence (green), combined with DAPI (blue) and MitoTracker (magenta) staining. Higher magnification images of the boxed area in B are shown in C.

(D) Amino acid sequence of the N-terminal domain of wt 11B and the indicated deletion mutants. Yellow, TOM20 recognition motif; blue, amphiphilic sequence.

(E) NIH-3T3 cells were transfected with wt 11B or the indicated mutants, followed 24 h later by 11B (magenta) and TOM20 (white) double immunofluorescence, combined with DAPI-staining (blue).

(F) Amino acid sequence of a fusion protein comprising the N-terminal 30 amino acids of 11B and EGFP. Yellow, TOM20 recognition motif; dark blue, amphiphilic sequence; light blue, linker sequence; green, EGFP (274, C-terminal amino acid).

(G) NIH-3T3 cells were transfected with the 11B1-30-EGFP fusion protein, followed 24 h later by GFP (green) and TOM20 (white) double immunofluorescence, combined with DAPI-staining (blue).

(H) NIH-3T3 cells were transfected with the 11B1-30-EGFP fusion protein, followed 24 h later by immunogold electron microscopy against GFP. Note the GFP immunoreactivity in the mitochondrial matrix.

(I) 11B (magenta), TOM20 (white) and SOX2 (cyan) triple immunofluorescence of the VZ of PCW10 human neocortex. Blue arrowheads indicate examples of 11B and TOM20 co-localization.

Scale bars, 10 μ m.

(J) GFP (green), TOM20 (white) and 11B (magenta) triple immunofluorescence of E14.5 mouse neocortex upon IUE at E13.5 with 11B and EGFP. Blue arrowheads indicate examples of 11B and TOM20 co-localization.

Fig. 2 Namba et al.

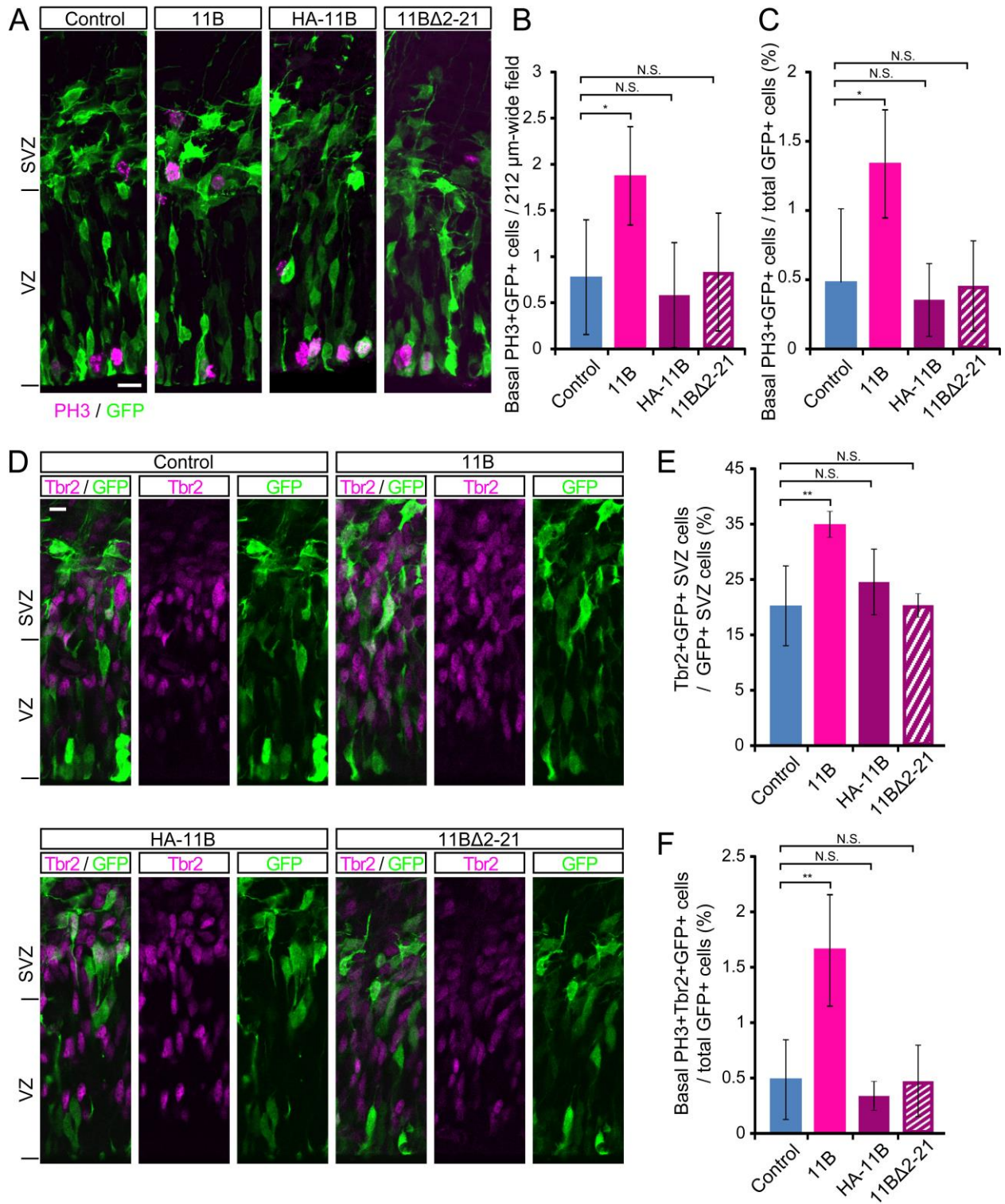


Figure 2. Mitochondrial localization of 11B is required for BP expansion.

IUE of neocortex of mouse E13.5 embryos with EGFP together with either empty vector (control), wt 11B, or the indicated 11B mutants, followed by analysis at E14.5.

(A) GFP (green) and phosphohistone H3 (PH3, magenta) double immunofluorescence.

5 (B, C) Quantification of basal PH3⁺ GFP⁺ cells, expressed either per 212 μ m-wide microscopic field (B, 12-24 fields used for quantification) or as a percentage of the total GFP⁺ cells in VZ, SVZ and apical portion of IZ (C). Blue, control; light magenta, 11B; dark magenta, HA-11B; dark magenta stripe, 11B Δ 2-21.

(D) GFP (green) and Tbr2 (magenta) double immunofluorescence.

10 (E) Quantification of Tbr2⁺ GFP⁺ SVZ cells as a percentage of total GFP⁺ SVZ cells.

(F) Quantification of basal PH3⁺ Tbr2⁺ GFP⁺ cells as a percentage of the total GFP⁺ cells in VZ, SVZ and apical portion of IZ.

Error bars, SD; *, $P < 0.05$; N.S., not statistically significant. For the number of cells counted, see Quantification and Statistical Analysis in STAR Methods. Scale bars, 10 μ m.

15

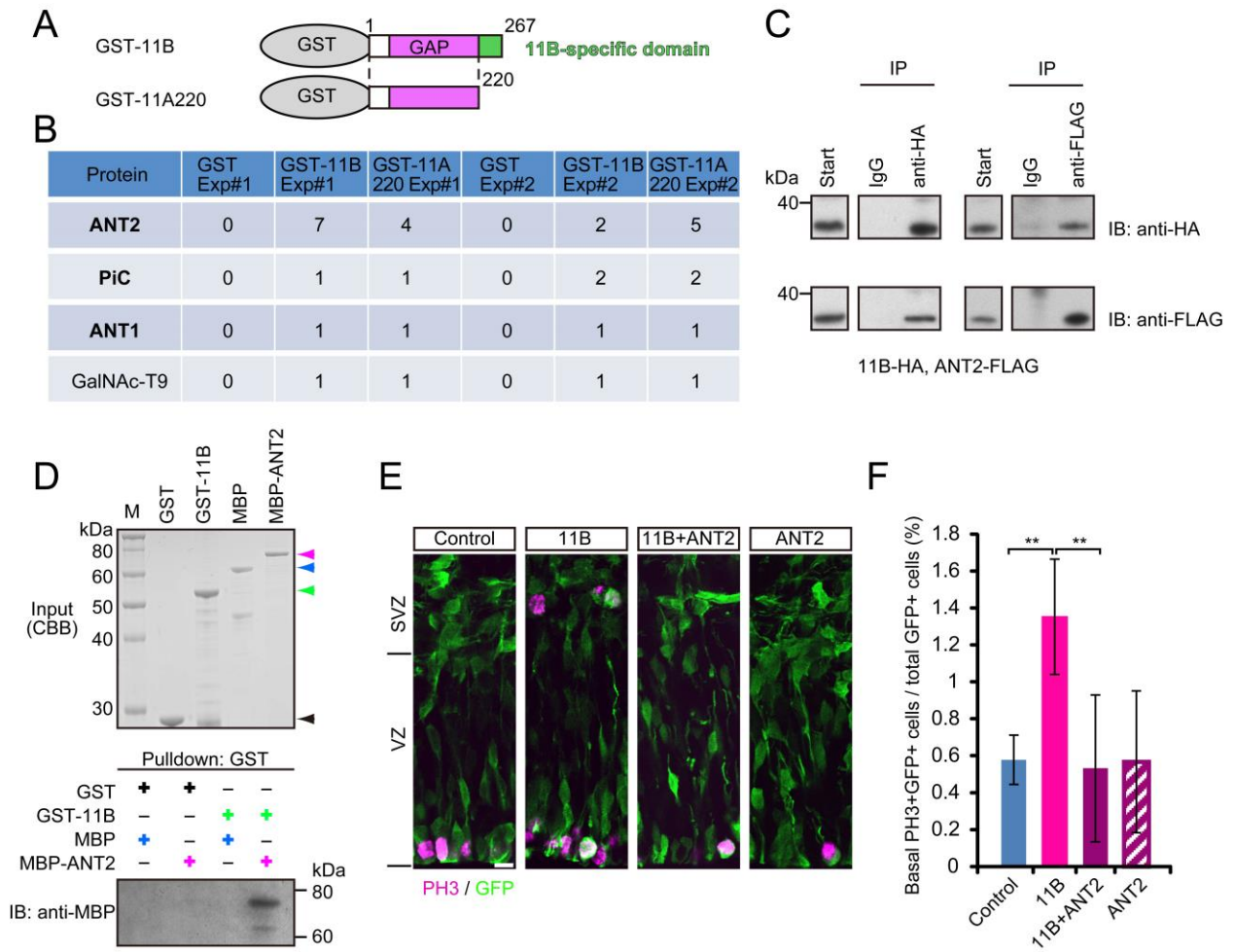


Figure 3. 11B interacts with ANT.

(A) Domain structure of GST-tagged 11B and 11A220 used for a pulldown assay. Gray, GST; magenta, truncated GAP domain; green, 11B-specific C-terminal domain. Numbers indicate the initiator methionine (1, left vertical dashed line), the end of the truncated GAP domain (220, right vertical dashed line), and the C-terminal amino acid of 11B (267).

(B) Proteins identified by mass spectrometry in pulldown assays using the indicated GST-tagged 11B and 11A220 proteins. Exp#1 and Exp#2, two independent pulldown assays. The numbers of the spectra unique for the respective protein are indicated. Proteins are listed in descending order by the number of unique spectra identified. Proteins in bold letters are located in the inner mitochondrial membrane. ANT2, adenine nucleotide translocator 2; PiC, phosphate carrier; ANT1, adenine nucleotide translocator 1; GalNAc-T9, polypeptide N-acetylgalactosaminyltransferase 9.

(C) COS-7 cells were transfected with 11B-HA and ANT2-FLAG, followed 24 h later by preparation of a cell lysate and immunoprecipitation (IP). IP was performed using anti-HA antibody (left panels) and anti-FLAG (right panels), followed by immunoblot (IB) analysis of the immunoprecipitates using anti-HA antibody (top panels) and anti-FLAG antibody (bottom panels). Molecular mass marker is indicated on the left.

(D) Top panel, Coomassie Brilliant Blue (CBB) staining of the SDS gel showing the recombinant proteins GST (black arrowhead), GST-11B (green arrowhead), MBP (blue arrowhead) and MBP-ANT2 (magenta arrowhead) used as input for the GST pulldown. Molecular mass markers (M) are shown on the left. Bottom panel, pulldown of GST and GST-tagged 11B from protein mixtures containing GST, GST-11B, MBP and MBP-ANT2 as indicated, followed by immunoblot (IB) analysis using anti-MBP antibody. Note the specific presence of MBP-ANT2

upon GST-11B pulldown, indicative of a direct 11B-ANT2 interaction. Molecular mass markers are indicated on the right.

5 (E, F) IUE of neocortex of mouse E13.5 embryos with EGFP together with either empty vector (control) or wt 11B and/or ANT2, followed by analysis at E14.5. (E) GFP (green) and PH3 (magenta) double immunofluorescence. (F) Percentage of basal GFP⁺ cells that are PH3⁺, upon control (blue), 11B (light magenta), 11B+ANT2 (dark magenta) and ANT2 (dark magenta stripe) IUE. Error bars, SD; **, $P < 0.01$. For the number of cells counted, see Quantification and Statistical Analysis in STAR Methods. Scale bar, 10 μm .

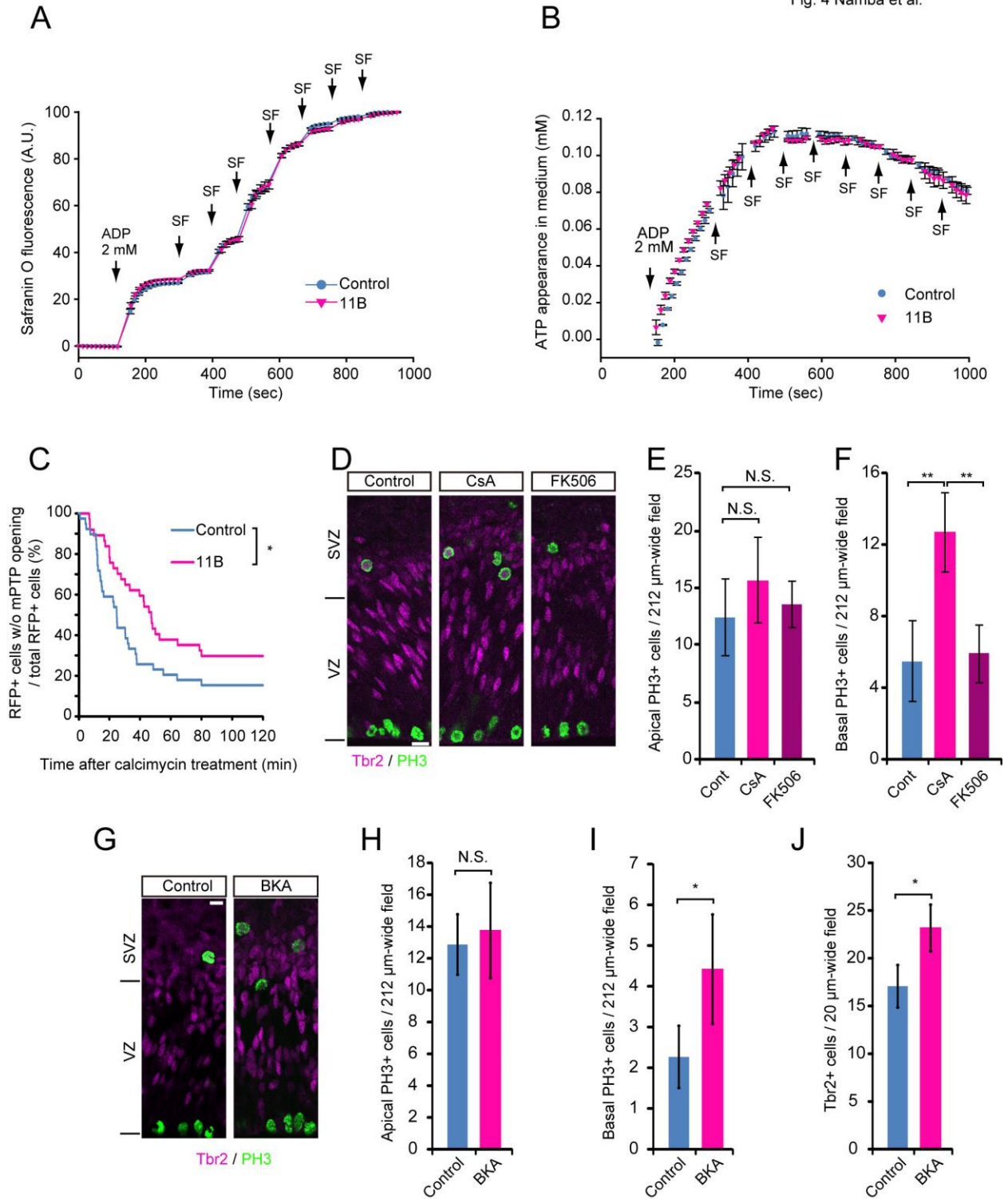


Figure 4. 11B delays mPTP onset but does not inhibit the ADP-ATP translocating activity of ANT.

(A) COS-7 cells were transfected with empty vector (control, blue) or 11B (magenta), followed 48 h later by cell permeabilization and measurement of safranin O fluorescence. Arrows indicate the time points of addition of ADP and the uncoupler SF6847 (SF, 10 nM). An increase in safranin O fluorescence indicates a depolarization of the mitochondrial membrane potential.

(B) COS-7 cells were transfected with empty vector (control, blue) or 11B (magenta), followed 48 h later by cell permeabilization and measurement of ATP appearance in the medium using Magnesium Green. Arrows indicate the time points of addition of ADP and SF6847 (SF, 10 nM).

(C) Percentage of RFP+ COS-7 cells that do not exhibit mPTP opening at the indicated time points after addition of calcimycin (see Figure S3A). Cells were transfected two days prior to analysis with an RFP targeted to mitochondria, together with either empty vector (control, blue) or 11B (magenta).

(D-F) Cerebral hemispheres of mouse E13.5 embryos were cultured for 24 h without (control) or with 4 μ M cyclosporin A (CsA) or FK506. (D) PH3 (green) and Tbr2 (magenta) double immunofluorescence of neocortex. (E, F) Quantification of apical (E) and basal (F) PH3+ cells in a 212 μ m-wide microscopic field of neocortex upon control (blue), CsA (light magenta) or FK506 (dark magenta) treatment. Twelve fields were used for each quantification.

(G-J) The lateral ventricles of mouse E13.5 embryos were *in utero* injected with PBS (control) or bongkreikic acid (BKA) in PBS, followed by analysis at E14.5. (G) PH3 (green) and Tbr2 (magenta) double immunofluorescence. (H-J) Quantification of apical (H) and basal (I) PH3+ cells in a 212 μ m-wide microscopic field, and of Tbr2+ cells in a 20 μ m-wide microscopic field (J), of control (blue) and BKA-administered (magenta) neocortex (15 and 12 fields used for quantification, respectively).

Error bars, SD; **, $P < 0.01$; *, $P < 0.05$; N.S., not statistically significant.

Scale bars, 10 μm .

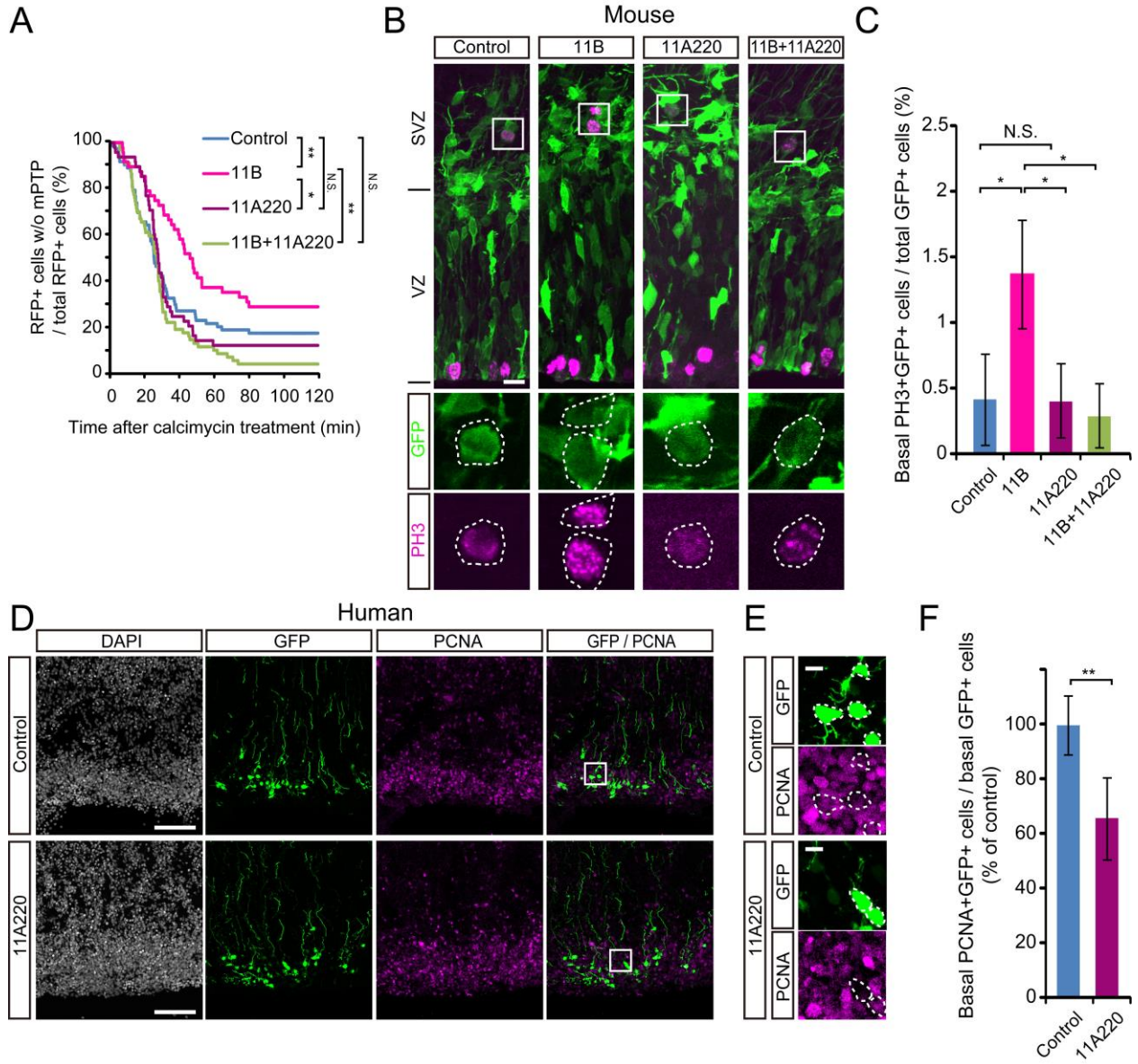


Figure 5. 11B inhibits mPTP via the 11B-specific domain.

(A) Percentage of RFP+ COS-7 cells that do not exhibit an mPTP at the indicated time points after addition of calcimycin. Cells were transfected two days prior to analysis with an RFP targeted to mitochondria, together with either empty vector (control, blue), 11B (light magenta), 11A220 (dark magenta) or 11B+11A220 (green).

(B, C) IUE of neocortex of mouse E13.5 embryos with EGFP together with either empty vector (control) or wt 11B and/or 11A220, followed by analysis at E14.5. (B) GFP (green) and PH3 (magenta) double immunofluorescence. Bottom panels, high magnification of the boxed areas in the top panels, showing either the GFP or the PH3 immunofluorescence. Dashed circles indicate PH3+ GFP+ cells. (C) Percentage of basal GFP+ cells that are PH3+, upon control (blue), 11B (light magenta), 11A220 (dark magenta) and 11B+11A220 (green) IUE.

(D-F) Neocortical tissue of human PCW11-14 fetus was electroporated with EGFP together with either empty vector (control) or 11A220, and cultured for three days. (D, E) GFP (green) and PCNA (magenta) double immunofluorescence, combined with DAPI staining (white), of PCW 13 neocortex. (E) High magnification of the boxed areas in D. (F) Quantification of GFP+ cells that are PCNA+, upon control (blue) and 11A220 (dark magenta) electroporation. The mean value for the control was set to 100%, and the mean value for 11A220 is expressed relative to this.

Error bars, SD; **, $P < 0.01$; *, $P < 0.05$; N.S., not statistically significant. For the number of cells counted, see Quantification and Statistical Analysis in STAR Methods.

Scale bars, 10 μm (B, E), 100 μm (D).

Fig. 6 Namba et al.

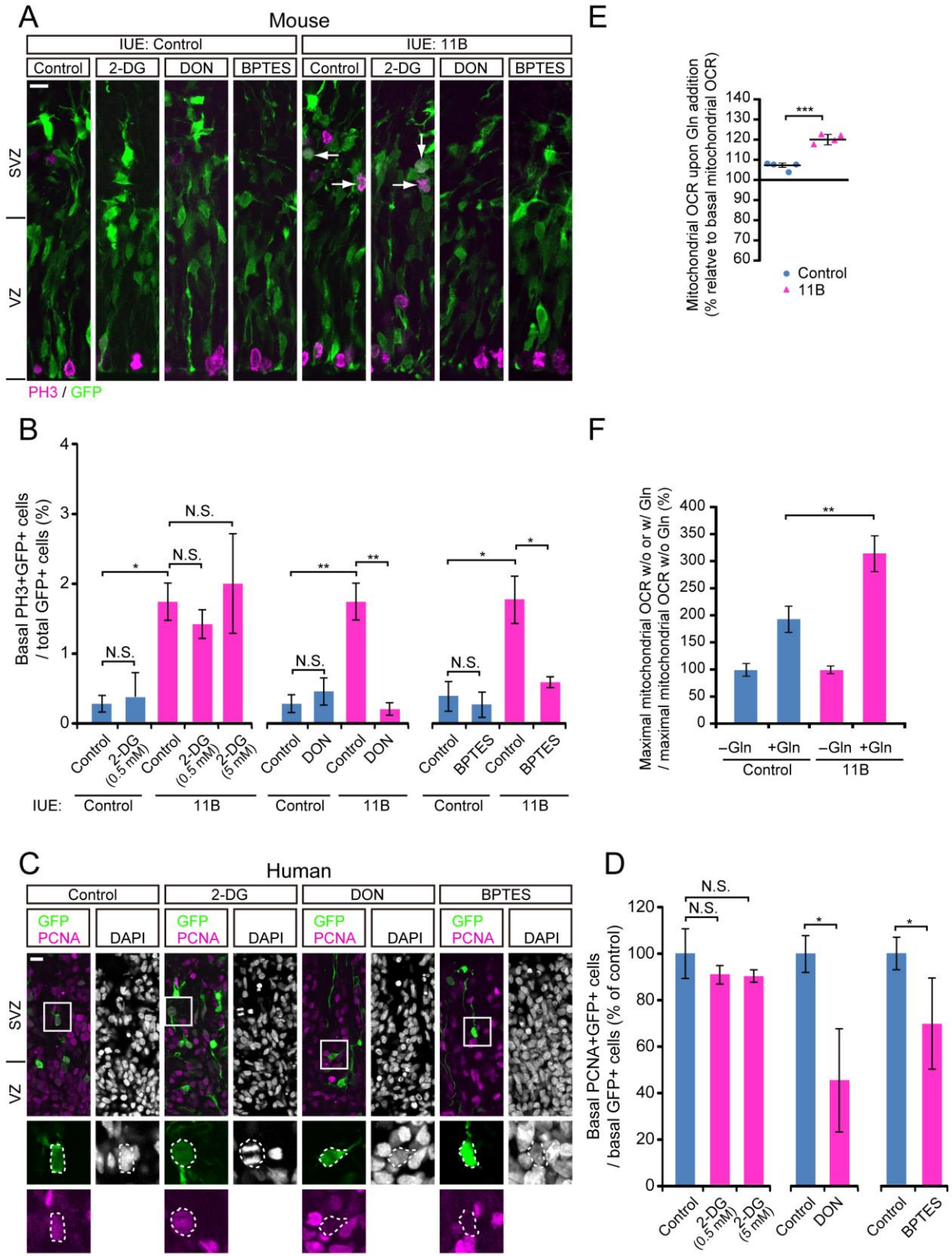


Figure 6. 11B promotes BP expansion via glutaminolysis.

(A, B) IUE of neocortex of mouse E13.5 embryos with EGFP together with either empty vector (Control) or 11B. Twelve hours after IUE, the cerebral hemispheres were dissected from the embryos and subjected for 12 h to HERO culture in the absence (Control) or presence of 0.5 mM (A, B) or 5 mM (B) 2-deoxyglucose (2-DG), 10 μ M 6-diazo-5-oxo-L-norleucine (DON), or 10 μ M bis-2-(5-phenylacetamido-1,3,4-thiadiazol-2-yl) ethyl sulfide (BPTES), as indicated. (A) GFP (green) and PH3 (magenta) double immunofluorescence. Scale bar, 10 μ m. (B) Percentage of total GFP⁺ cells that are PH3⁺ in a basal location, upon control (blue) or 11B (magenta) IUE followed by treatment in HERO culture as indicated.

(C, D) Neocortical tissue of human PCW11-13 fetuses was electroporated with EGFP and subjected to FFT culture for one day without treatments. The tissue was then further cultured for 2 days in the absence (Control) or presence of 0.5 mM (C, D) or 5 mM (D) 2-DG, 10 μ M DON, or 20 μ M BPTES, as indicated. (C) GFP (green) and PCNA (magenta) double

immunofluorescence, combined with DAPI staining (white), of PCW11 neocortical tissue.

Bottom panels, high magnification of the boxed areas in the top panels, showing either the GFP, PCNA or DAPI (immuno)fluorescence. Dashed circles indicate GFP⁺ cells that are either PCNA⁺ or PCNA⁻. (D) Quantification of basal GFP⁺ cells that are PCNA⁺, with treatments as indicated. The mean values for the control were set to 100%, and the mean values for the indicated treatments are expressed relative to these.

(E, F) Mitochondrial oxygen consumption rate (OCR) measured by the Seahorse analyzer. COS-7 cells were transfected with either empty vector (Control) or 11B two days prior to analyses. (E) Mitochondrial OCR after the addition of 10 mM galactose and 2 mM glutamine (Gln) is expressed as a percentage of the basal mitochondrial OCR (set to 100%, horizontal line), that is,

prior to the addition of the substrates. Blue, control; magenta, 11B. **(F)** Maximal mitochondrial OCR in the presence of 2 μM of the ATP synthase inhibitor oligomycin, 100 μM of the uncoupler 2,4-dinitrophenol (DNP), 10 mM glucose and 2 mM glutamine (+Gln) is expressed relative to the maximal mitochondrial OCR measured in the presence of oligomycin, DNP and glucose but absence of glutamine (-Gln). The mean values for the latter were set to 100%, and the mean values for the maximal mitochondrial OCR in the presence of glutamine are expressed relative to these. Blue, Control; magenta, 11B.

Error bars, SEM, **(B)**, SD **(D, E, F)**. ***, $P < 0.001$; **, $P < 0.01$; *, $P < 0.05$; N.S., not statistically significant. For the number of cells counted, see Quantification and Statistical Analysis in STAR Methods.

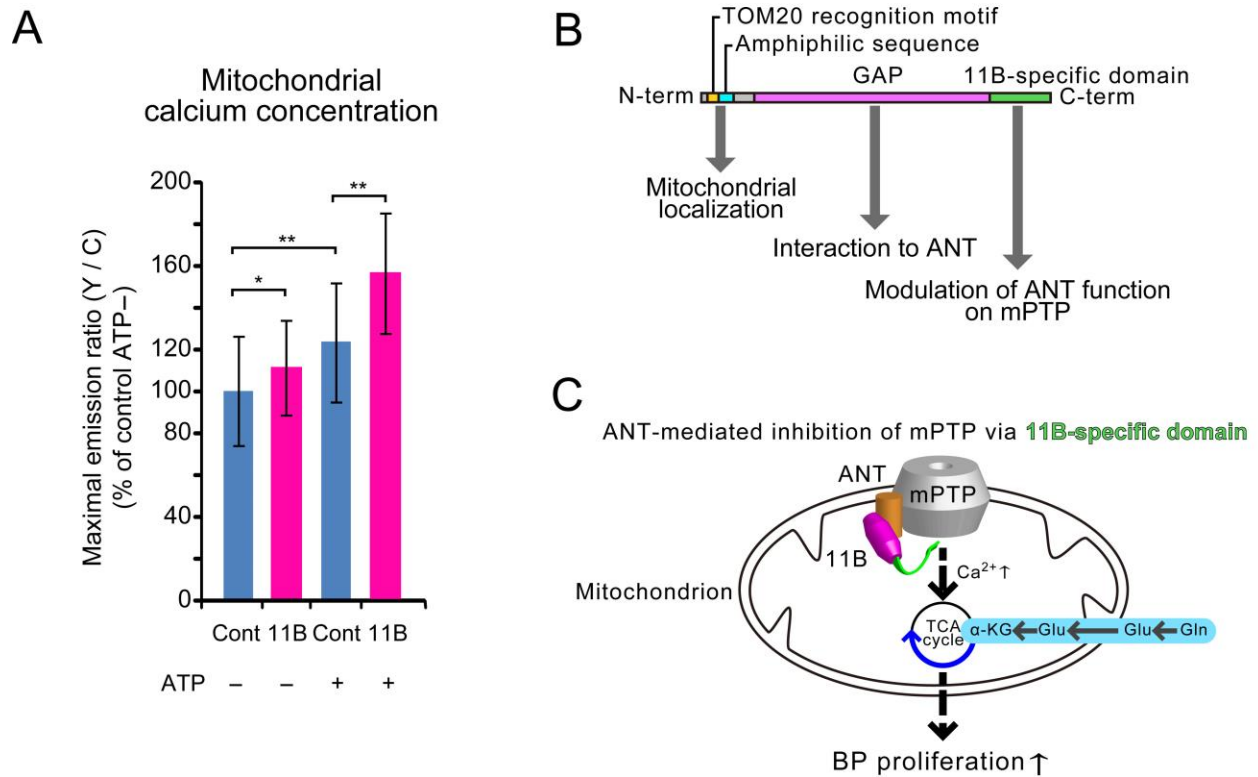


Figure 7. 11B increases mitochondrial calcium concentration, and model of 11B action in mitochondria.

(A) Analysis of mitochondrial calcium concentration. COS-7 cells were transfected two days prior to analysis with the FRET-based calcium indicator 4mtD3cpV targeted to mitochondria, together with empty vector (control (Cont), blue) or 11B (magenta). Cells were treated without (-) or with (+) extracellular ATP to induce an elevation of cytosolic calcium. Maximal yellow and cyan (Y/C) emission ratios are indicated on the ordinate axis. The mean value for the control without ATP treatment was set to 100%, and the mean values for the other conditions are expressed relative to this. Error bars, SD; *, $P < 0.05$; **, $P < 0.01$.

(B) 11B domains and their molecular function. 11B contains three functional domains. The N-terminal domain is required and sufficient for mitochondrial localization (yellow, TOM20 recognition motif; blue, amphiphilic sequence). The middle domain, encompassing the truncated

GAP domain (magenta) that does not exhibit RhoA-GAP activity *in vivo*, mediates the interaction of 11B with ANT. The C-terminal domain, which comprises the 47 amino acid human-specific sequence (green), modulates ANT function on mPTP.

(C) Model of 11B function in mitochondria and its link to glutaminolysis. 11B is localized in the inner mitochondrial membrane and/or matrix and interacts with ANT (brown) through its truncated GAP domain (magenta). Via this interaction, the 11B-specific domain (green) is able to delay mPTP (gray) opening. The inhibition of mPTP allows mitochondria to acquire a higher calcium concentration in the matrix. Increased mitochondrial calcium is known to activate α -ketoglutarate dehydrogenase, the enzyme catalyzing the conversion of α -ketoglutarate (α -KG) to succinyl-CoA, thereby increasing the progression of the TCA cycle from α -ketoglutarate onwards (blue line of TCA cycle). This ultimately results in 11B-expressing BPs to exhibit higher proliferative capacity, which is thought to underlie the expansion of the human neocortex. An essential basis for this 11B-induced process is provided by glutaminolysis, the conversion of glutamine (Gln) to glutamate (Glu) to α -KG (blue), as this metabolic pathway increases α -KG levels.

STAR Methods

CONTACT FOR REAGENT AND RESOURCE SHARING

Further information and requests for resources and reagents should be directed to the Lead
5 Contact, Wieland Huttner (huttner@mpi-cbg.de).

EXPERIMENTAL MODEL AND SUBJECT DETAILS

Ethics

All animal experiments were performed in accordance with the German Animal Welfare
10 legislation (“Tierschutzgesetz”). All procedures regarding the animal experiments were approved
by the Governmental IACUC (“Landesdirektion Sachsen”) and overseen by the Institutional
Animal Welfare Officer(s). The license numbers concerning the experiments with mice are:
Untersuchungen zur Neurogenese in Mäuseembryonen TVV2015/05 (in utero electroporation)
and 24–9168.24-9/2012-1 (tissue collection without prior in vivo experimentation).

Mice

C57BL/6J mice were used for all experiments using mouse tissue. Balb/c mice were used for
anti-ARHGAP11B antibody and anti-Tbr2 antibody production. Mice were maintained in
pathogen-free conditions at the animal facility of the Max Planck Institute of Molecular Cell
20 Biology and Genetics (MPI-CBG) or in JANVIER LABS, France. All experiments were
performed in accordance with German animal welfare legislation and were overseen by the
Institutional Animal Welfare Officer. Necessary licenses were obtained from the regional Ethical
Commission for Animal Experimentation of Dresden, Germany (Tierversuchskommission,
Landesdirektion Dresden).

Human tissues

Fetal human brain tissue (PCW10-14) was obtained from the Klinik und Poliklinik für
Frauenheilkunde und Geburtshilfe, Universitätsklinikum Carl Gustav Carus of the Technische
Universität Dresden, with approval of the local University Hospital Ethical Review Committees
30 and from the Human Development Biology Resource (HDBR), with the fetal human material

being provided by the Joint MRC/Wellcome Trust (MR/R006237/1) Human Developmental Biology Resource (www.hdbr.org).

5 Fetal human brain tissues obtained from Dresden were dissected in PBS and used immediately for further manipulation or fixation. Tissues obtained from HDBR were dissected and shipped in Hibernate E media (Gibco A1247601). Upon arrival, the tissue was cultured in slice culture medium (SCM, see the following section) for 6-12 h prior to any further manipulation.

METHOD DETAILS

Plasmids

10 pCAGGS-ARHGAP11B, -HA-ARHGAP11B and -EGFP have been described previously (Florio et al., 2015; Florio et al., 2016). pDsRed2-Mito was obtained from Clontech. Full length *ARHGAP11A*, *ARGAP11A220*, *ARHGAP11BΔ2-21*, *ARHGAP11BΔ2-12*, and mouse *Slc25a5* (ANT2) were first cloned into pCR-Blunt II-TOPO (Invitrogen), and then subcloned into
15 pCAGGS to obtain pCAGGS-ARHGAP11A, -ARHGAP11A220, -ARHGAP11BΔ2-21, -ARHGAP11BΔ2-12, and -mSlc25a5. *ARHGAP11B*, *ARHGAP11A220*, *ARHGAP11A250* and *ancARHGAP11B-NLS-mt* were first cloned into pCR-Blunt II-TOPO, and then subcloned into pCAGGS-C'HA to obtain pCAGGS-ARHGAP11B-HA, -ARHGAP11A220-HA, -ARHGAP11A250-HA, -ancARHGAP11B-HA and -ancARHGAP11B-NLS-mt-HA.
20 *ARHGAP11B1-30* was first cloned into pCR-Blunt II-TOPO, and then subcloned into pEGFP-N3 (Clontech) to obtain pEGFP-N3-ARHGAP11B1-30. *ARGAP11A220*, *ARHGAP11B* and *ARHGAP11B221-267* were first cloned into pCR-Blunt II-TOPO, and then subcloned into pGEX-6P-1 (Promega) to obtain pGEX-6P-ARHGAP11A220, -ARHGAP11B and -ARHGAP11B221-267. Mouse *Slc25a5* (ANT2) was first cloned into pCR-Blunt II-TOPO, and
25 then subcloned into p3XFLAG-CMV-14 (Sigma) to obtain pCMV-mSlc25a5-3xFLAG. Mouse *Slc25a5* cDNA was amplified by PCR and subcloned into pOCC102 to obtain pOCC102-mSlc25a5.

Antibodies

30 Antibodies used in this study were as follows; anti-ARHGAP11A (rabbit IgG, ab113261, Abcam), anti-ARHGAP11B (mouse IgG₁, 3758-A37-5, MPI-CBG), anti-FLAG (mouse IgG,

F1084, Sigma), anti-GFP (goat IgG, MPI-CBG), anti-HA (rabbit IgG, 3724, Cell Signaling Technology), anti-GFP (rabbit IgG, ab290, Abcam), anti-GFP (rat IgG, 1867423, Roche), anti-PCNA (mouse IgG, CBL407, Millipore), anti-PH3 (rat, ab10543, Abcam), anti-SOX2 (goat IgG, SC-17320, Santa Cruz Biotechnology), anti-Tbr2 (mouse IgG₁, 3815-A12-1, MPI-CBG), anti-Tbr2 (mrabbit IgG, Gift from Robert Hevner (Englund et al., 2005)), anti-TOM20 (rabbit IgG, ab78547, Abcam), anti-TOM20 (rabbit IgG, SC-11415, Santa Cruz Biotechnology), anti-TOM20 (mouse IgG, ab56783, Abcam), anti-goat IgG-Alexa Fluor 488 (donkey, A11055, ThermoFisher Scientific), anti-goat IgG-Alexa Fluor 647 (donkey, A21447, ThermoFisher Scientific), anti-mouse IgG-Alexa Fluor 488 (donkey, A21202, ThermoFisher Scientific), anti-mouse IgG-Alexa Fluor 555 (donkey, A31570, ThermoFisher Scientific), anti-mouse IgG-Alexa Fluor 647 (donkey, A31571, ThermoFisher Scientific), anti-mouse IgG-HRP (goat, 115-035-068, Jackson ImmunoResearch), anti-rabbit IgG-Alexa Fluor 488 (donkey, A21206, ThermoFisher Scientific), anti-rabbit IgG-Alexa Fluor 647 (donkey, A31573, ThermoFisher Scientific), anti-rabbit IgG-HRP (donkey, 711-035-152, Jackson ImmunoResearch), anti-rat IgG-Alexa Fluor 488 (donkey, A21208, ThermoFisher Scientific), anti-rat IgG-Cy3 (donkey, 712-165-153, Jackson ImmunoResearch), normal mouse IgG (015-000-003, Jackson ImmunoResearch) and normal rat IgG (ab326, Abcam).

To produce anti-ARHGAP11B and anti-Tbr2 antibodies, mice were injected with peptides (KLH-conjugated CKALKKVNMKLLVNIREREDNV for 11B; biotin-conjugated KRKRLSPSTPSNGNSPPIKCEDINTEEYSKDTSKGMGAYYAFYTSP for Tbr2) together with adjuvant. Isolated splenocytes from the immunized mice were fused to myeloma cells to create hybridomas. Supernatants of hybridomas were collected and purified by HiTrap Protein G column (GE Healthcare). For anti-ARHGAP11B antibody, the purified antibody was passed through a HiTrap NHS-activated HP column (GE Healthcare) in which E15.5 mouse brain lysate was coupled to reduce non-specific binding.

Cell transfection

NIH-3T3 cells were transfected with indicated plasmids (1 µg per transfection) by Lipofectamine 2000 (Invitrogen) according to the manufacturer's protocol. COS-7 cells were transfected with indicated plasmids (1-2.5 µg per transfection) by Amaxa nucleofector (Lonza) or by

Lipofectamine 2000 according to the manufacturer's protocols. Cells were cultured in cell growth medium (DMEM (Invitrogen) supplemented with 10% FBS and 1x Penicillin-Streptomycin (Invitrogen)) at 37°C under an atmosphere of humidified 5% CO₂ and 95% air.

5 Immunocytochemistry

NIH-3T3 cells cultured on PDL-coated coverslips were fixed with 3.7% formalin for 15 min, 24 h after the transfection. Then cells were washed with PBS and incubated with 0.1 M glycine in PBS for 30 min at room temperature (r.t.), followed by incubation with a mixture of the indicated primary antibodies in PBS containing 1% bovine serum albumin (BSA, Sigma) and 0.1% Triton X-100 for 1-2 h at r.t.. Cell were washed with PBS and then incubated with a mixture of appropriate secondary antibodies and DAPI (Sigma) for 1 h at r.t., and washed again with PBS before being mounted on microscopy slides with Mowiol.

15 Immunoelectron microscopy

NIH-3T3 cells cultured on 5 cm dishes were fixed with 4 % paraformaldehyde (PFA) at 24 h post transfection, washed with PBS and 0.1% (w/v) glycine, and then incubated with 12% gelatine in 0.1 M phosphate buffer at 37°C. Cells were gently scraped from the petridish and the cell suspension was centrifuged at 1000 rpm for 5 min. The solidified cell pellet was cut into small cubes, which were incubated with 2 M sucrose/15% PVP for Tokuyasu cryosectioning (70 nm). Sections were prepared and immunolabelled as previously described (Paridaen et al., 2015), using rabbit antibodies against GFP (Abcam). Detection of the primary antibodies for EM was carried out with proteinA/10-nm-gold (University Utrecht). The grids were thoroughly washed with water before negative contrasting with a mixture of 1.9% methyl cellulose/0.3% uranyl acetate for 10 min on ice. Images were taken on a Morgagni EM at 80 kV (FEI) with a Morada camera and ITEM software (EMSIS).

25 In utero electroporation (IUE) of embryonic mouse neocortex

IUE was performed as previously described (Namba et al., 2014). Briefly, pregnant mice with E13.5 embryos were anesthetized with isoflurane, followed by subcutaneous injection with the analgesic (0.1 ml, Metamizol, 200 mg/kg). Using a glass micropipette the embryos were injected intraventricularly with a solution containing 0.1% Fast Green (Sigma) in sterile 154 mM NaCl, 1

5 $\mu\text{g}/\mu\text{l}$ of the pCAGGS plasmid (empty vector, ARHGAP11B and its indicated mutants, ARHGAP11A220 and/or ANT2) and 0.3 $\mu\text{g}/\mu\text{l}$ of the EGFP vector, followed by electroporation (24 V, five 50 msec pulses with 950 msec intervals). After surgery mice received Metamizol for one day via drinking water (1.33 mg/ml). Mice were sacrificed by cervical dislocation and embryos were harvested 20-24 h post-electroporation, and the embryonic brains were dissected and PFA-fixed for immunohistochemistry (see below).

In utero intraventricular injection into mouse embryos

10 *In utero* intraventricular injection of bongkreikic acid (BKA) was performed as previously described (Yung et al., 2011), with minor modifications. Briefly, pregnant mice with E13.5 embryos were anesthetized with isofluorane, followed by subcutaneous injection with the analgesic (0.1 ml, Metamizol, 200 mg/kg). Using a glass micropipette the embryos were injected intraventricularly with a solution containing 0.1% Fast Green (Sigma) with or without (control) 0.9 mM BKA in sterile PBS. After surgery mice received Metamizol for one day via drinking
15 water (1.33 mg/ml). Mice were sacrificed by cervical dislocation and embryos were harvested 20-24 h post-injection, and the embryonic brains were dissected and PFA-fixed for immunohistochemistry (see below).

Mouse cerebral hemisphere culture

20 Cerebral hemispheres were dissected from E13.5 mouse embryos not subjected to IUE, or from E14.0 mouse embryos 12 h after IUE at E13.5, and placed in the hemisphere rotation (HERO) culture as previously described (Schenk et al., 2009), with minor modifications. Hemispheres were cultured with slice culture medium (SCM; Neurobasal medium (Invitrogen) supplemented with 20 mM L-glutamine (Invitrogen), 1x Penicillin-Streptomycin (Invitrogen), 1x N2
25 supplement (Invitrogen), 1x B27 supplement (Invitrogen), 0.1 mM HEPES-NaOH (pH 7.3) and 10% rat serum (Charles River Japan)). Depending on the substance to be added, the SCM contained either (i) 0.1% ethanol (control), 4 μM cyclosporine A (CsA; 4 mM stock dissolved in ethanol; Sigma) or 4 μM FK-506 (4 mM stock dissolved in ethanol; Sigma), followed by incubation for 20-24 h; or (ii) 0.1% PBS (control for 2-DG and DON), 0.5 mM or 5 mM 2-
30 deoxyglucose (2-DG; 500 mM or 5M stock dissolved in PBS; Sigma), 10 μM 6-diazo-5-oxo-L-norleucine (DON; 10 mM stock dissolved in PBS; Sigma), or 0.1% DMSO (control for BPTES)

or 10 μ M bis-2-(5-phenylacetamido-1,3,4-thiadiazol-2-yl) ethyl sulfide (BPTES, 10 mM stock dissolved in DMSO), followed by incubation for 12 h at 37°C under an atmosphere of humidified 5% CO₂, 40% O₂ and 55% N₂. The hemispheres were then PFA-fixed for immunohistochemistry, or were processed for the PPIase assay (see below).

5

Human tissue electroporation and free-floating tissue (FFT) culture

Ex vivo electroporation of the fetal human neocortical tissue was performed as described previously (Kalebic et al., 2019) for **Figure 5D-F**, or using a newly-developed system (see **Figure S6**) for **Figure 6C, D** and **Figure S5**, as follows. Neocortical tissue was placed onto a spoon-shaped anode filled with sterile PBS. Then, the mixture of plasmids (pCAGGS-EGFP at 1 μ g/ μ l together with pCAGGS empty vector at 2 μ g/ μ l for control or pCAGGS-ARHGAP11A220 at 2 μ g/ μ l), in a solution containing 0.1% Fast Green (Sigma), 5% glycerol and PBS, was added onto the apical surface of the tissue. The cathode was placed on top of the PBS-covered tissue, and electroporations were performed using 36-40 V and five 50 msec pulses with 950 msec intervals, with the plasmid DNA entering cells in the apical-to-basal direction. After the electroporation, the tissue was washed in PBS, placed into a rotating flask with 1.5 ml human SCM, and incubated as FFT culture (Long et al., 2018) at 37°C for 3 days in a humidified atmosphere of 5% CO₂, 60% O₂ and 35% N₂ before being fixed.

10

15

20

Immunohistochemistry

For GFP/PH3, GFP/Tbr2, Tbr2/PH3 and GFP/PCNA double immunofluorescence, 14 μ m-thick cryosections were stained as described previously (Vaid et al., 2018).

25

For ARHGAP11B/TOM20/GFP triple immunofluorescence of mouse electroporated neocortex, 14 μ m-thick cryosections were incubated in 0.01 M Na-citrate buffer for 60 min at 70 °C, followed by incubation for 20 min at r.t. for antigen retrieval. Then sections were washed with PBS and incubated with 0.1 M glycine in PBS for 30 min at r.t., followed by permeabilization with a solution containing 0.2% (wt/vol) gelatin, 300 mM NaCl and 0.3% (wt/vol) Triton X-100 in PBS (TX buffer) for 30 min at r.t.. Subsequently sections were incubated with a solution containing 1% BSA and 1% fetal calf serum in PBS for 30 min at r.t.. The sections were then incubated with the mixture of primary antibodies in Can Get Signal immunostain

30

Immunoreaction Enhancer Solution B (TOYOBO) for 24 h at 4°C. Sections were washed with PBS followed by an incubation with a mixture of appropriate secondary antibodies in Can Get Signal immunostain Immunoreaction Enhancer Solution B for 1 h at r.t. and washed again with PBS before being mounted on microscopy slides with Mowiol.

5

For ARHGAP11B/TOM20/SOX2 or ARHGAP11B/TBR2/SOX2 triple immunofluorescence of fetal human neocortex, 14 µm-thick cryosections were incubated in 0.01 M Na-citrate buffer for 60 min at 70 °C, followed by incubation for 20 min at r.t. for antigen retrieval. Then sections were permeabilized in PBS containing 0.3% Triton X-100 for 30 min at r.t., followed by incubation with 0.1 M glycine in PBS for 30 min at r.t.. Subsequently sections were incubated with 10% horse serum in PBS for 60 min at r.t.. The sections were then incubated with a mixture of the primary antibodies in PBS containing 10% horse serum for 24 h at 4°C. Sections were washed with PBS followed by incubation with a mixture of appropriate secondary antibodies in PBS containing 10% horse serum for 1 h at r.t., and washed again with PBS before being mounted on microscopy slides with Mowiol.

10

15

Image acquisition and quantification

The fluorescent images were acquired using LSM700 and LSM 880, with 40x and 63x objectives. Images were taken as either 1.2-µm (40x) or 0.5 µm (63x) single optical sections.

20

When the images were taken as tile scans, the images were stitched together using the ZEN software (Zeiss).

Quantifications were performed using the ZEN software and Fiji. Any PH3+ cell 30 µm from the apical surface and any GFP+PCNA+ cell lacking apical contact and 30 µm from the apical surface was counted as a BP. Note that most of the basal PH3+ cells were located in SVZ.

25

Peptidylprolylisomerase (PPIase) assay

PPIase assay was performed as described previously with minor modifications (Folda et al., 2016). The cultured hemispheres were collected and subjected to one cycle of freezing-thawing.

30

The tissue was then homogenized in 50 mM HEPES/Tris (pH 8.0), 100 mM NaCl and 1% Tween 20. The homogenate was centrifuged at 5,000 g for 10 min at 4°C, and the resulting supernatant

used further. Protein concentration in the supernatant was determined using the BCA kit (ThermoFisher Scientific). Fifty μg protein each of the 5,000 g supernatant were incubated with 0.25% ethanol (control) or 5 μM CsA in 0.25% ethanol, in 50 mM HEPES/Tris (pH 8.0) and 100 mM NaCl at 4°C for 15 min. The assay was performed at 9°C after addition of α -chymotrypsin (dissolved in 1 mM HCl, final concentration 4.8 μM , Sigma-Aldrich), followed 1 min later by addition of N-succinyl-Ala-Ala-Pro-Phe-*p*-nitroanilide (final concentration 6 μM , Sigma-Aldrich; dissolved in trifluoroethanol containing 470 mM LiCl). The absorbance at 405 nm was measured by GENios Pro (TECAN) at 6 sec intervals for up to 177 sec. The data obtained were subjected to background subtraction (reactions with 0.25% ethanol, α -chymotrypsin and N-succinyl-Ala-Ala-Pro-Phe-*p*-nitroanilide but without 5,000 g supernatant), and then fitted to a zero-order rate equation in order to obtain the PPIase rate constants.

Calcineurin assay

Cytoplasmic calcineurin activity was measured using the FRET-based calcineurin activity sensor Cyto-CaNAR2 (Mehta et al., 2014). E13.5 mouse neocortex was subjected to IUE as above, using 1 $\mu\text{g}/\mu\text{l}$ of pcDNA3-Cyto-CaNAR2. Cerebral hemispheres were dissected immediately after IUE and cultured for 24 h with ethanol (control), CsA or FK506 as described above in Mouse cerebral hemisphere culture. After the HERO culture, the hemispheres were sectioned into 300-400 μm - thick slices, and the slices were placed onto a collagen-coated glass-bottom dish.

The YFP/CFP FRET signal was measured using an LSM700 and analyzed using Fiji.

Recombinant protein production

For GST, GST-11B, GST-11A220 and GST-11B221-267 recombinant proteins, T7 Express competent *E. coli* was transformed with pGEX-6P-1, pGEX-6P-ARHGAP11B, pGEX-6P-ARHGAP11A220 or pGEX-6P-ARHGAP11B221-267, respectively, and cultured for 20 h at 18°C with IPTG (0.2 mM), ampicillin (100 mcl/ml) and chloramphenicol (100 mcl/ml). For each recombinant protein, respective cells were harvested and re-suspended in the *E. coli* lysis buffer A (2x PBS, 1 mM MgCl_2 , 1 mM DTT and benzonase), and disrupted by Emulsiflex. Lysate was centrifuged at 16,000g for 30 min and the supernatant was loaded on a GSTrap-FF column, followed by washing with PBS containing 1 mM DTT. Trapped proteins were eluted by 2x PBS

containing 5 mM reduced glutathione and 1 mM DTT, followed by dialysis in 2x PBS containing 10% glycerol and 1 mM DTT, and kept at -80°C for a long-term storage.

5 For MBP and MBP-ANT2 recombinant proteins that contain His6-tag, T7 Express competent *E. coli* was transformed with pOCC102 or pOCC102-mSlc25a5, and cultured for 20 h at 18°C with IPTG (0.2 mM), ampicillin (100 mcg/ml) and chloramphenicol (100 mcg/ml). For each recombinant protein, respective cells were harvested and re-suspended in the *E. coli* lysis buffer B (2xPBS, 10 mM imidazole, 1 mM MgCl₂, 1 mM DTT and benzonase), and disrupted by Emulsiflex. Lysate was centrifuged at 16,000g for 30 min and the supernatant was loaded on a
10 HisTrap column followed by washing with 2x PBS containing 10 mM imidazole, 1 mM MgCl₂ and 1 mM DTT. Bound proteins were eluted by 2x PBS containing 250 mM imidazole, followed by dialysis in a buffer containing 50 mM Tris-HCl, 300 mM NaCl, 1.25 mM MgCl₂, 10% glycerol, 0.5% NP-40 and 1 mM DTT, and kept at -80°C for a long-term storage.

15 Pulldown assay

Cerebral hemispheres of E15.5 mice were homogenized in the tissue lysis buffer (50 mM Tris-HCl, 200 mM NaCl, 1% NP-40, cComplete Protease Inhibitor Cocktail (Roche) and PhosSTOP (Roche)) by BioMasher Standard (Takara) and sonication, and then incubated with magnetic
20 Glutathione beads (ThermoFisher Scientific) for 1 h at 4°C with gentle rotation. Subsequently the lysate was centrifuged at 15,000g for 10 min at 4°C, and the supernatant was incubated with GST, GST-11B or GST-11A220 recombinant proteins for 1 h at 4°C with gentle rotation, followed by an addition of magnetic glutathione beads and further incubation for 1 h at 4°C with gentle rotation. Beads were collected by a magnetic stand and washed with the tissue lysis buffer. Finally 11B or 11A220 and their interacting proteins were eluted by 3C protease cleavage in the
25 3C buffer (50 mM TrisHCl, 1 mM EGTA, 150 mM NaCl, 1% NP-40 and 1 mM DTT) overnight at 4°C. Supernatants were processed for mass spectrometry (see below).

30 Indicated combination of recombinant proteins (GST, GST-11B, MBP and/or MBP-ANT2) were incubated with Glutathione Sepharose 4B (GE Healthcare) in binding assay buffer (50 mM Tris-HCl, 150 mM NaCl, 0.5% NP-40, 1 mM DTT and cComplete Protease Inhibitor Cocktail) for 1 h at 4°C. The beads were washed with binding assay buffer, and bound proteins finally eluted by

1x SDS sample buffer (57 mM Tris-HCl, 2.8% SDS, 5.7% glycerol, 0.0028% bromophenol blue) with 2-mercaptoethanol (1.7%), followed by incubation at 99°C for 10 min and processing for immunoblot analysis (see below).

5 Mass spectrometry

The method of mass spectrometry has been described elsewhere. Briefly, the GST pulldown samples are first processed for SDS-PAGE and then gels were incubated in Coomassie staining solution (50% methanol, 10% acetic acid, 0.2% CBB R-250) followed by washing in de-staining solution (50% methanol, 2% acetic acid). Coomassie-stained gel lanes were cut into 10 pieces per
10 lane, each of which was then individually processed for in-gel digestion of proteins by trypsin. The digested peptides were analyzed by a nano-UPLC Ultimate 3000 interfaced on-line to a Velos LTQ Orbitrap hybrid mass spectrometer (both Thermo Fischer Scientific, Bremen). Acquired spectra were searched against mouse sequences in the UniProt database (January 2018) using MASCOT software (version 2.2.04, 50 Matrix Sciences Ltd, London, UK). The results of
15 the database searches were evaluated by Scaffold software v.4.8.7 (Proteome Software, Portland). Protein hits were accepted if matched with one peptide under 95% probability thresholds for both peptides and proteins. Proteins and peptide False Discovery Rates (FDR, function of the Scaffold software) were calculated below 0.8% and 1%, respectively. We excluded tubulins and ribosomal proteins to obtain the interacting protein list.

20

Immunoprecipitation

COS-7 cells co-transfected with pCAGGS-ARHGAP11B-HA and pCMV-mSlc25a5-3xFLAG were harvested at 24 h post-transfection and lysed in cell lysis buffer (50 mM Tris-HCl, 150 mM NaCl, 1% Triton X-100, 0.1% SDS and cOmplete Protease Inhibitor Cocktail) by sonication, and
25 then incubated with Protein G Sepharose 4 Fast Flow (GE Healthcare) for 1 h at 4°C with gentle rotation. Subsequently the lysate was centrifuged at 15,000g for 10 min at 4°C, and the supernatant was incubated with normal rat IgG, rat anti-HA antibody, normal mouse IgG or mouse anti-FLAG antibody for 1 h at 4°C with gentle rotation, followed by addition of Protein G Sepharose 4 Fast Flow and further incubation for 1 h at 4°C with gentle rotation. Beads were
30 collected by centrifugation (800g) and washed with cell lysis buffer. Finally immunoprecipitated

proteins were eluted by 1x SDS sample buffer with 2-mercaptoethanol, followed by incubation at 99°C for 10 min and processing for immunoblot analysis (see below).

Immunoblot analysis

5 SDS-PAGE was performed using Novex Bis-Tris Gels (4-12%; ThermoFisher Scientific) in NuPAGE MOPS SDS Running Buffer (ThermoFisher Scientific) according to the manufacturer's protocol. Then proteins were transferred onto PVDF membrane (Immobilon-P, Merck) in NuPAGE Transfer Buffer (ThermoFisher Scientific) for 2 h. The membranes were incubated in TBST (Tris-buffered saline containing 0.1% Tween 20) containing 5% BSA or in PVDF
10 Blocking Reagent for Can Get Signal (TOYOBO; only for anti-11B antibody) for 1 h at r.t. with gentle shaking, followed by incubation with the indicated primary antibodies in TBST or in Can Get Signal Immunoreaction Enhancer Solution (TOYOBO; only for anti-11B antibody) overnight at 4°C with gentle shaking. The membranes were washed with TBST and then incubated with appropriate HRP-conjugated secondary antibodies in TBST or in Can Get Signal
15 Immunoreaction Enhancer Solution (only for anti-11B antibody) for 1 h at r.t. with gentle shaking. Finally membranes were developed with SuperSignal West Dura Extended Duration Substrate (ThermoFisher Scientific). Exposure time to X-ray film was varied for best visibility. Images were acquired using PERFECTION V750 PRO (EPSON).

ADP/ATP translocation analysis

20 Mitochondrial membrane potential ($\Delta\Psi_m$) determination in *in situ* mitochondria of permeabilized COS-7 cells: $\Delta\Psi_m$ was estimated using fluorescence quenching of the cationic dye safranin O due to its accumulation inside energized mitochondria (Akerman and Wikstrom, 1976), with the considerations applicable to permeabilized cells as outlined in Kawamata et al. (Kawamata et al.,
25 2010). COS-7 cells were treated exactly as described for $[Mg^{2+}]$ free determination, except that magnesium green (MgG) was replaced by 5 μ M safranin O. Fluorescence was recorded in a Spectramax M5 plate reader at one acquisition every 10 sec plus 1 sec for mixing in between each acquisition, using 495 and 585 nm excitation and emission wavelengths, respectively. Experiments were performed at 37°C.

30

[Mg²⁺] free determination from Magnesium Green fluorescence in the experimental volume containing permeabilized COS-7 cells and conversion to ADP-ATP exchange rate: COS-7 cells from a T75 cm² flask (~70-80% confluent), resuspended in 0.7 ml of a buffer containing (in mM): KCl 8, K-gluconate 110, NaCl 10, HEPES-NaOH 10, KH₂PO₄ 10, EGTA 0.005, mannitol 10, MgCl₂ 1.5 and 0.5 mg/ml bovine serum albumin (fatty acid-free), pH 7.25 plus glutamate 5, malate 5, Ap5A 0.1, NaF 5, BeSO₄ 0.2 and Na₃VO₄ 0.025, were distributed into three wells of a white opaque 96 well flat-bottom plate. Digitonin (7 µl of 2.5 mM, dissolved in bi-distilled water) and MgG 5K⁺ salt (1 µM) were subsequently added. MgG fluorescence was recorded in a Spectramax M5 plate reader (Molecular Devices, Sunnyvale, CA 94089, USA) at one acquisition every 10 sec plus 1 sec for mixing in between each acquisition, using 505 and 535 nm excitation and emission wavelengths, respectively. Experiments were performed at 37 °C. Mitochondrial phosphorylation was started by the addition of 2 mM ADP. ADP-ATP exchange rate was estimated using the method by Chinopoulos et al. (Chinopoulos et al., 2009) exploiting the differential affinity of ADP and ATP to Mg²⁺ with the modifications outlined in Kawamata et al. (Kawamata et al., 2010). The rate of ATP appearing in the medium following addition of ADP to energized mitochondria (or vice versa in case of sufficiently de-energized mitochondria), is calculated from the measured rate of change in free extramitochondrial [Mg²⁺] using the following equation:

$$[ATP]_t = \frac{[Mg^{2+}]_t - 1 - \frac{[ADP]_t(t=0) + [ATP]_t(t=0)}{K_{ADP} + [Mg^{2+}]_t}}{[Mg^{2+}]_f} \bigg/ \frac{1}{K_{ATP} + [Mg^{2+}]_f} - \frac{1}{K_{ADP} + [Mg^{2+}]_f}$$

Here, [ADP]_t and [ATP]_t are the total concentrations of ADP and ATP, respectively, in the medium, and [ADP]_{t(t=0)} and [ATP]_{t(t=0)} are [ADP]_t and [ATP]_t in the medium at time zero. For the calculation of [ATP] or [ADP] from free [Mg²⁺], the apparent K_d values are identical to those in Chinopoulos et al. (Chinopoulos et al., 2009) due to identical experimental conditions (K_{ADP}=0.906 ± 0.023 mM, and K_{ATP}=0.114 ± 0.005 mM). The presence of NaF, BeSO₄ or Na₃VO₄ did not alter these K_d values, nor the K_d of Mg²⁺ for MgG, or the MgG fluorescence signal itself (not shown). [Mg²⁺]_t is the total amount of Mg²⁺ present in the media. Equation 1 is available for download as an excel file at:

[http://antactivity.com/Conversion_of_\[Mg2\]free_to_\[ATP\].html](http://antactivity.com/Conversion_of_[Mg2]free_to_[ATP].html).

mPTP opening analysis

Time lapse epifluorescence microscopy was carried out at 34°C to image COS-7 cells transfected two days prior to analyses with pDsRed2-Mito and indicated plasmids and swelling of *in situ* mitochondria was measured by the thinness ratio (TR) technique exactly as described in Gerencser et al. (Gerencser et al., 2008). Basically, cells were imaged directly on the LabTek chamber without superfusion in a medium containing (in mM): 120 NaCl, 3.5 KCl, 1.3 CaCl₂, 20 HEPES-NaOH, 15 glucose at pH 7.4. Experiments were performed on an Olympus IX81 inverted microscope equipped with a 60x 1.4 NA oil immersion lens, a Bioprecision-2 xy-stage (Ludl Electronic Products Ltd.) and a 75W xenon arc lamp (Lambda LS, Sutter Instruments, Novato, CA). For DsRed2, a 535/20 nm exciter, a 555LP dichroic mirror and a 570LP emitter (Omega Optical) were used. Time lapses of z-series of 16 planes of 512×512 pixels frames (digitized at 14bit with no binning, 250 ms exposure time, yielding 0.1 μm pixel size and 0.8 μm z-spacing) were acquired using an ORCA-ER2 cooled digital CCD camera (Hamamatsu Photonics) under control of MetaMorph 6.0 software (Molecular Devices; Sunnyvale, CA, USA). The TR technique measures changes of average diameters of thread-like or punctate structures in fluorescence images using a pair of (high and low frequency) bandpass spatial filters. A calibration image series of DsRed2 fluorescence showing mitochondrial swelling by valinomycin (200 nM) was recorded and used to train a spatial bandpass filter set in Image Analyst MKII (Image Analyst Software, Novato, CA). To calculate TR, the z-stack for each time point was mean-intensity projected and the projection image was duplicated. Then both images were spatially filtered and the absolute value of pixels was taken. The TR was calculated as the ratio of the average fluorescence intensity in the high frequency bandpass filtered image over the low frequency bandpass filtered image. Mitochondrial swelling causes the loss of high spatial frequency image details and therefore a decrease in the TR value. Baseline normalized TR is given as $\delta TR = (TR - TR_0) / TR_0$.

Mitochondrial calcium imaging

Time-lapse epifluorescence microscopy was carried out to image cells expressing the mitochondria-targeted FRET-based calcium indicator 4mtD3cpV (Palmer and Tsien, 2006) as described previously (Doczi et al., 2016). Specifically, transfected COS-7 cells plated on a

LabTek chamber were imaged in a medium (without superfusion) containing (in mM): 120 NaCl, 3.5 KCl, 1.3 CaCl₂, 15 glucose, 20 HEPES- NaOH at pH 7.4. Experiments were performed at 34°C on an Olympus IX81 inverted microscope equipped with a 60 × 1.4 NA oil immersion lens, a Bioprecision-2 xy-stage (Ludl Electronic Products Ltd., Hawthorne, NY) and a 75W xenon arc lamp (Lambda LS, Sutter Instruments, Novato, CA). For 4mtD3cpV imaging, the following filter sets were used: a 440/20 exciter, a dual bandpass (450–490 nm and 520–560 nm transmitting) dichroic mirror, a 480/10 emitter for CFP (CFP channel) and 535/20 emitter for YFP variant (FRET channel), all from Chroma Technology Corp., Bellows Falls, VT. Time lapses of 1344 × 1024 pixel frames for both channels (digitized at 14 bit with no binning, 400 msec exposure times) were acquired using an ORCA-ER2 cooled digital CCD camera (Hamamatsu Photonics, Hamamatsu, Japan) under control of MetaMorph 6.0 software (Molecular Devices; Sunnyvale, CA, USA). Image Analyst MKII software (Image Analyst Software, Novato, CA) was used for image analysis.

Oxygen consumption rate (OCR) measurement

We performed OCR measurement using the Seahorse XF96 extra cellular flux analyzer (Agilent Technologies) as described previously (Nemeth et al., 2016) with minor modifications. COS-7 cells at one day post-transfection were plated onto PDL-coated XF96 Cell Culture Plate (Agilent Technologies) at 40,000 cells / well, and cultured in cell growth medium for 20-24 h.

Subsequently cells were washed gently with Seahorse XF medium (Agilent Technologies) two times, and then incubated in the same medium for 1 h at 37°C without additional CO₂ supply. Then the OCR was measured in Seahorse XF medium under the following conditions; first without additions, and then with the sequential additions of (i) 10 mM glucose, 10 mM galactose and/or 2 mM glutamine, (ii) 10 mM oligomycin (Agilent Technologies), (iii) 100 μM 2,4-dinitrophenol (DNP, Sigma), and (iv) 1 μM antimycin A (Agilent Technologies) plus 1 μM rotenone (Agilent Technologies) (A+R). All measurements were performed at 37°C under air without additional CO₂ supply. Data were normalized to total protein content measured by the BCA protein assay kit (ThermoFisher Scientific) and subsequently analyzed by Wave (Agilent Technologies). Each data point consists of triplicate or quadruplicate measurements. Before calculating the following parameters, non-mitochondrial OCR (the OCR after the addition of A+R) was subtracted from the other OCR values. To calculate (i) basal mitochondrial OCR

(OCR prior to substrate addition), (ii) external substrate-induced mitochondrial OCR (OCR after substrate addition) and (iii) maximal mitochondrial OCR (OCR after addition of oligomycin and DNP), the average of 4 to 5 time points was determined.

5 Hydrogen Deuterium Exchange Mass Spectrometry (HDX-MS) and structural modeling

HDX-MS was performed essentially as previously described (He et al., 2015; Mayne et al., 2011; Walters et al., 2012). Proteins were diluted 6:4 with 8 M urea, 1% trifluoroacetic acid, and passed over a column with immobilized pepsin (2.1 mm x 30 mm, ThermoFisher Scientific) in 0.1% trifluoroacetic acid, 5% methanol at 15°C. Peptides were captured on a reversed-phase C8
10 cartridge, desalted and separated by a Zorbax 300SB-C18 column (Agilent) at 1°C using a 5-40% acetonitrile gradient containing 0.1% formic acid over 12 min and electrosprayed directly into an Orbitrap mass spectrometer (LTQ-Orbitrap XL, ThermoFisher Scientific) with a T-piece split flow setup (1:400). Data were collected in profile mode with source parameters: spray voltage 3.4 kV, capillary voltage 40 V, tube lens 170 V, capillary temperature 170°C. Where applicable,
15 MS/MS CID fragment ions were detected in centroid mode with an AGC target value of 104. CID fragmentation was 35% normalized collision energy (NCE) for 30 ms at Q of 0.25. HCD fragmentation NCE was 35 eV. Peptides were identified using Mascot (Matrix Science) and manually verified to remove ambiguous peptides. For measurement of deuterium uptake, protein was diluted 1:9 in 20 mM Tris-HCl (pH 7.5), 150 mM NaCl, 5 mM MgCl₂, prepared in
20 deuterated solvent. Samples were incubated at 22°C, followed by the aforementioned digestion, desalting, separation and mass spectrometry steps. The intensity weighted average m/z value of a peptide's isotopic envelope was compared plus and minus deuteration using the HDX workbench software platform (Pascal et al., 2012). Individual peptides were verified by manual inspection. Deuterium uptake was normalized for back-exchange by comparing deuterium uptake to a
25 sample incubated in 6 M urea, 1.2 μM pepsin, 10 mM NaH₂PO₄ prepared in deuterated buffer for 12-18 h at r.t. and processed as indicated above. Molecular models were generated using the iTASSER server (Zhang, 2008). While all 5 models were in general agreement, we used the model which best reflected the deuterium uptake profile.

30

QUANTIFICATION AND STATISTICAL ANALYSIS

Quantification

Quantifications were performed using the ZEN software and Fiji. Any PH3+ cell 30 μ m from the apical surface and any GFP+PCNA+ cell lacking apical contact and 30 μ m from the apical surface was counted as a BP. Note that most of the basal PH3+ cells were located in SVZ. The SVZ was defined as the region with rounded and less densely packed nuclei.

Statistical analysis

Data were analyzed with Excel (Microsoft, Redmond, WA), Statcel3 (OMS, Japan), MYSTAT (Systat Software, CA) and SigmaPlot (Systat Software). Statistical tests: Tukey-Kramer method was used for multiple groups of observations that follow a normal distribution with equal variances (**Figure 2B, C, F; Figure 3F; Figure 4F; Figure 6B** (control vs DON), **F; Figure S4A, B**) Scheffe's F test was used for multiple groups of observations regardless their distributions and variances (**Figure 2E; Figure 4E; Figure 5C; Figure 6B** (control; vs 2-DG, control vs BPTES), **D** (control vs 2-DG); **Figure 7A; Figure S3B, C; Figure S5B**). Mann-Whitney U-test was used for two groups of observations that do not follow a normal distribution (**Figure 4H; Figure 6D** (control vs DON); **Figure S5C**), two-tailed Student's t-test was used for two groups of observations that follow a normal distribution with equal variances (**Figure 4I, J; Figure 5F; Figure 6D** (control vs BPTES), **E**). Kaplan-Meier estimate followed by the Logrank test with the Bonferroni correction was used for **Figure 4C, Figure 5A**. The Shapiro-Wilk normality test or the F test or the Bartlett's test was used for testing normality or homoscedasticity of all samples. Results were interpreted as statistically significant when $P < 0.05$.

Sample sizes of experiments were as follows; **Figure 2B** (control, $n = 6$; 11B, $n = 8$; HA-11B, $n = 4$; 11B Δ 2-21, $n = 4$ embryos), **Figure 2C** (control, $n = 5$; 11B, $n = 6$; HA-11B, $n = 4$; 11B Δ 2-21, $n = 4$ embryos, in total 1372 – 2620 GFP+ cells/group were counted), **Figure 2E** ($n = 4$ embryos, in total 189 – 262 GFP+ cells/group were counted), **Figure 2E** ($n = 4$ embryos, in total 1633 – 1958 GFP+ cells/group were counted), **Figure 3F** ($n = 5$ embryos for each group, in total 1948 – 1285 GFP+ cells/group were counted), **Figure 4A, B** ($n = 3$ experiments for each group), **Figure 4C** (control, $n = 39$; 11B, $n = 37$ cells), **Figure 4E, F** ($n = 4$ embryos for each group, in total 149 – 188 (for **E**) and 66 – 153 (for **F**) PH3+ cells/group were counted), **Figure 4H-J** (control, $n = 5$; BKA, $n = 4$ embryos, in total 165 and 193 (for **H**) and 34 – 53 (for **I**) PH3+ cells

and in total 256 and 278 Tbr2+ cells (for **J**) /group were counted), **Figure 5A, Figure S3B, C** (control, n = 74; 11B, n = 48; 11A220, n = 48; 11B+11A220, n = 67 cells), **Figure 5C** (control, n = 4; 11B, n = 4; 11A220, n = 4; 11B+11A220, n = 3 embryos, in total 1077 – 1869 GFP+ cells/group were counted), **Figure 5F** (n = 4 fetus for each group, in total 249 and 273 GFP+ cells/group were counted), **Figure 6B** (Control IUE +PBS, n = 7; Control IUE +2-DG, n = 4; Control IUE +DON, n = 4; Control IUE +DMSO, n = 3; Control IUE +BPTES, n = 4; 11B IUE +PBS, n = 8; 11B IUE +0.5 mM 2-DG, n = 3; 11B IUE +5 mM 2-DG, n = 3; 11B IUE +DON, n = 4; 11B IUE +DMSO, n = 4; 11B IUE +BPTES, n = 3 hemispheres, in total 582 – 3229 GFP+ cells/group were counted), **Figure 6D** (PBS, n = 3; 0.5 mM 2-DG, n = 3; 5 mM 2-DG, n = 3; DON, n = 3; DMSO, n = 4; BPTES, n = 4 fetus, in total 71 and 149 GFP+ cells/group were counted), **Figure 6E, F** (n = 4 experiments for each group), **Figure 7A** (control ATP-, n = 112; 11B ATP-, n = 138; control ATP+, n = 58; 11B ATP+, n = 76 cells), **Figure S4A** (n = 4 experiments for each group), **Figure S4B** (n = 26 cells for each group), **Figure S5B, C** (n = 3 hemispheres for each group, in total 49 – 65 GFP+ cells/group were counted).

15

Supplementary Text

Structural differences between 11A and 11B

We further explored mechanisms underlying the differential subcellular localization of different mutants of 11A and 11B (as listed in Figure S1A). To this end, NIH-3T3 cells were transfected with indicated plasmids (**Figure S1D, E**). We found that short truncated mutants of 11A (11A220 and 11A250) were localized in mitochondria as revealed by counter-immunostaining for TOM20 (**Figure S1D**). In contrast, ancestral 11B (anc11B) (Florio et al., 2016), which has a slightly longer C-terminal sequence containing one NLS, is mainly localized in the nucleus (**Figure S1E**). This result raised two possible mechanisms that explain nuclear, but not mitochondrial, localization of 11A; 1) NLS in the C-terminal sequence is dominant over the mitochondria-targeting sequence; 2) 11A C-terminal sequence somehow masks its N-terminal mitochondria-targeting sequence. Because anc11B with mutated NLS (anc11B-NLS-mt) was excluded from the nucleus but was still not localized in mitochondria (**Figure S1E**), NLS does not seem to be dominant over the mitochondria-targeting sequence.

We therefore examined the 3D structure of 11A and 11B. The structure of 11A GAP domain, as determined previously (Protein Data Bank [PDB] ID code 3EAP), shows that the protein sequence following the GAP domain in 11A is sterically close to its N-terminal domain, raising the possibility that the long C-terminal sequence following the GAP domain affects the structure of the mitochondria-targeting sequence or physically masks the sequence. Since the structure of 11B has not been determined yet, we predicted its 3D structure using iTASSER with verification by Hydrogen deuterium exchange mass spectrometry (HDX-MS). Of the five predicted models, we chose the one based on HDX-MS analysis (**Figure S1F**). Interestingly, in this 11B model, although the 11B C-terminal sequence is completely different from that of 11A250, the N-terminal and C-terminal regions are close together. The mitochondria-targeting sequence was shown to be exposed on the surface of 11B, and therefore might be accessible to mitochondrial import receptors. In conclusion, the difference in the subcellular localization of 11B and 11A might depend on the accessibility of the mitochondria-targeting sequence.

Validation of anti-11B antibody

We have validated our newly developed anti-11B mAb in three different ways. First, by immunoblot of HA-11A or HA-11B expressing COS-7 cells, the antibody was shown to recognize only HA-11B but not HA-11A (**Figure S2A**). Second, in mouse neocortex at E14.5, the antibody exclusively stained the GFP+ cells upon 11B electroporation but not the GFP+ cells upon empty vector electroporation (**Figure S2B**). Third, the immunofluorescence signals of anti-11B antibody in the PCW10 human neocortex (**Figure 1I, Figure S2C, D**) were largely abolished when the antibody was pre-incubated with the recombinant protein that covers the immunogen (**Figure S2E, F**).

10

Fig. S1 Namba et al.

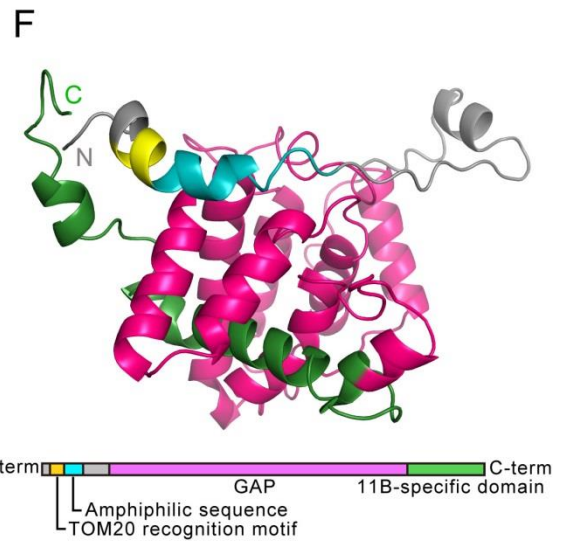
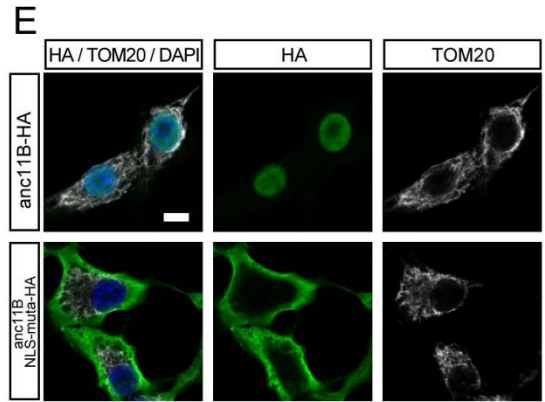
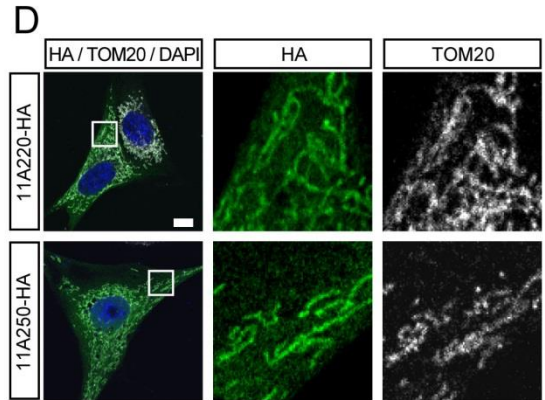
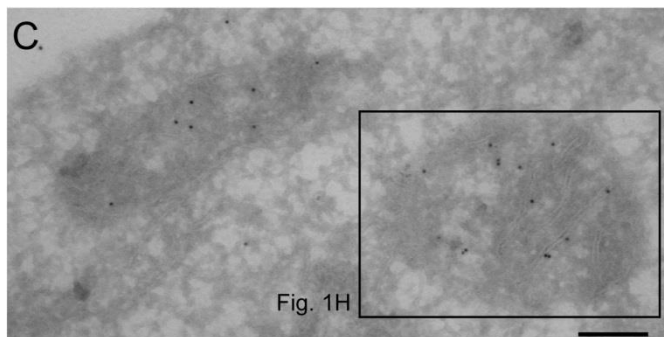
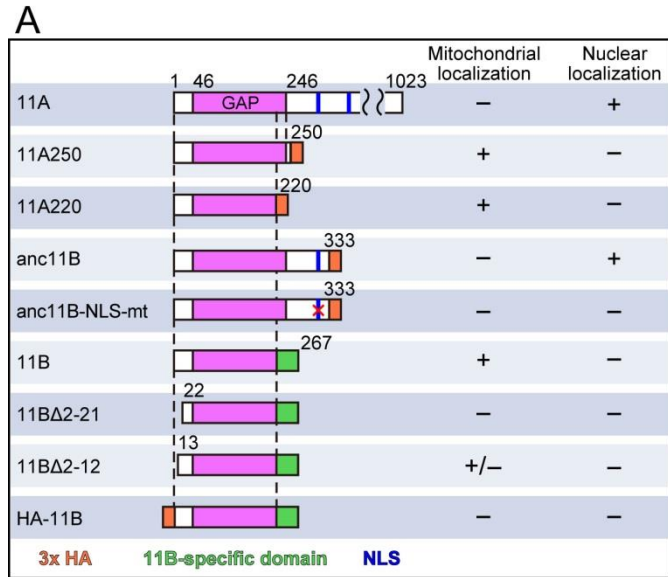


Figure S1. The N-terminal mitochondria-targeting sequence present in 11A and 11B is masked in full-length 11A.

(A) Domain structures and summary of mitochondrial vs. nuclear localization of wt 11A and its indicated mutants, of wt anc11B and its indicated mutant, and of wt 11B and its indicated mutants. Magenta, GAP domain; orange, 3x HA-tag; green, 11B-specific domain comprising the 47 amino acid human-specific C-terminal sequence; blue, nuclear localization signal (NLS).

Numbers indicate the initiator methionine (1, left vertical dashed line), the beginning (46) and end (246) of the GAP domain, the C-terminal amino acid of 11A (1023), anc11B (333) and 11B (267), and the N-terminal amino acid of 11B Δ 2-21 (22) and 11B Δ 2-12 (13); the two right vertical dashed lines indicate amino acid residues 220 and 246, respectively. The red cross at the NLS of anc11B-NLS-mt indicates the mutation of the NLS (KRKRR to AAAAA).

(B, C) NIH-3T3 cells were transfected with the 11B1-30-EGFP fusion protein, followed 24 h later by immunogold electron microscopy. The boxed area in B is shown at higher magnification in C, and the boxed area in C is shown at higher magnification in **Figure 1H**. Note the GFP immunoreactivity in the mitochondrial matrix.

(D) NIH-3T3 cells were transfected with 11A220-HA or 11A250-HA, followed 24 h later by HA (green) and TOM20 (white) double immunofluorescence, combined with DAPI-staining (blue). The boxed areas in the merge images are shown at higher magnification as single channel images on the right. Note that both 11A220 and 11A250 are localized in mitochondria.

(E) NIH-3T3 cells were transfected with anc11B-HA or anc11B-NLS-mt-HA, followed 24 h later by HA (green) and TOM20 (white) double immunofluorescence, combined with DAPI-staining (blue). Note that anc11B is localized in the nucleus but that anc11B-NLS-mt shows a cytoplasmic localization. Neither of the two proteins is localized in mitochondria.

(F) Top: 3D structural model of 11B as predicted by I-TASSER by incorporating information from the X-ray crystallographic structure of the 11A GAP domain. This 11B model was verified by HDX-MS analysis. Bottom: Domain structure of 11B. Domain colors correspond to the colors in the 3D structural model of 11B shown on top; yellow, TOM20 recognition motif; blue, amphiphilic sequence; magenta, GAP domain; green 11B-specific C-terminal domain. Note that the N-terminus and C-terminus of 11B are close together and that the TOM20 recognition motif and the amphiphilic sequence are exposed on the surface.

Scale bars, 240 nm (B, C), 10 μ m (D, E).

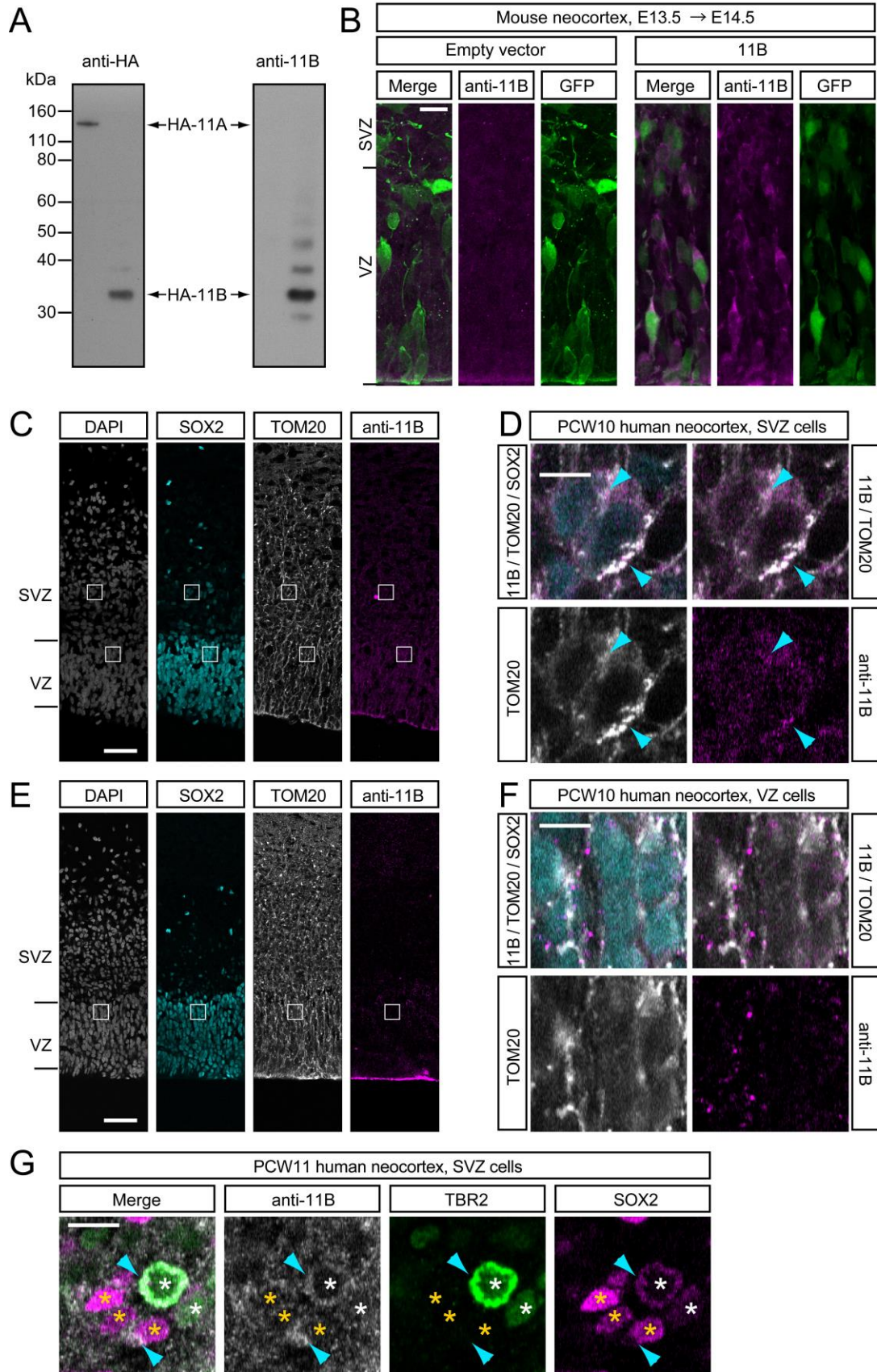


Figure S2. Validation of the anti-11B mAb.

(A) Immunoblots of COS-7 cells transfected 24 h prior to analysis with HA-11A (left lanes) or HA-11B (right lanes), using either anti-HA antibody (left blot) or the anti-11B mAb (right blot). Note that the anti-11B mAb does not react with 11A.

5 (B) GFP (green) and 11B (magenta) double immunofluorescence of E14.5 mouse neocortex after IUE at E13.5 of EGFP together with empty vector (left panels) or 11B (right panels). Note the absence and presence of specific 11B immunoreactivity in the control neocortex and 11B-electroporated neocortex, respectively.

10 (C, D) 11B (magenta), TOM20 (white) and SOX2 (cyan) triple immunofluorescence of PCW10 human neocortex, combined with DAPI-staining (blue in left panel of C). Higher magnification images of the boxed areas in C are shown in D (SVZ) and in **Figure 1J** (VZ). Cyan arrowheads in D indicate examples of 11B and TOM20 co-localization.

15 (E, F) 11B (magenta), TOM20 (white) and SOX2 (cyan) triple immunofluorescence of PCW10 human neocortex, combined with DAPI-staining (blue in left panel of E). Prior to use, the 11B mAb was pre-incubated with recombinant GST-11B221-267 fusion protein, which contains the peptide sequence of the immunogen (11B247-267) used to raise the anti-11B mAb. Higher magnification images of the boxed area of the VZ in E are shown in F.

20 (G) 11B (white), TBR2 (green) and SOX2 (magenta) triple immunofluorescence of SVZ of PCW11 human neocortex. Cyan arrowheads indicate examples of 11B expression in cytoplasm. White asterisks and yellow asterisks indicate TBR2⁺ SOX2⁺ and TBR2⁻ SOX2⁺ nuclei, respectively.

Scale bars, 10 μ m (B, G), 50 μ m (C, E), 5 μ m (D, F).

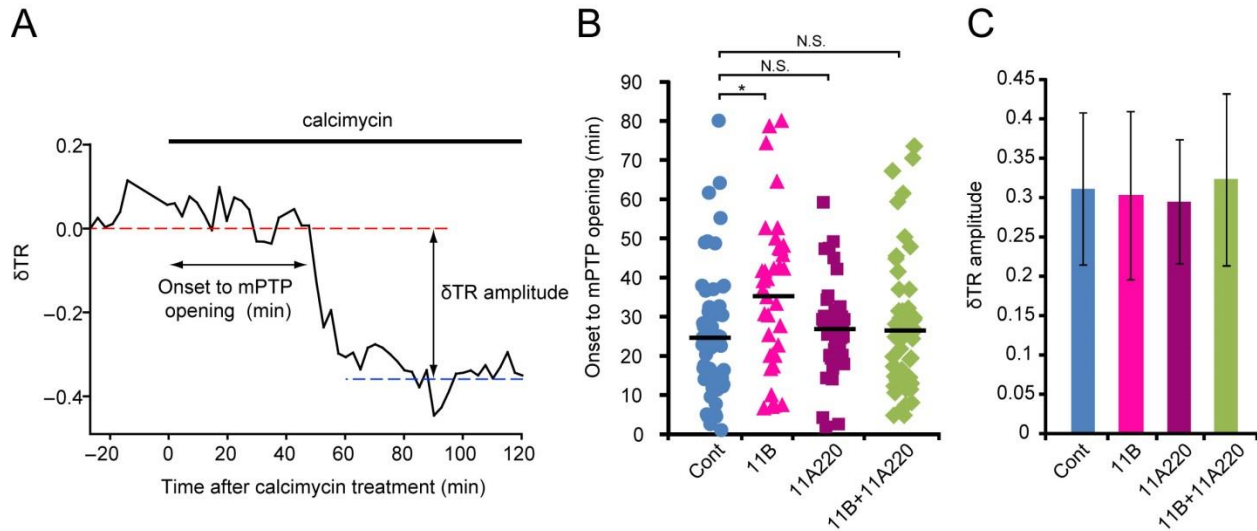


Figure S3. 11B delays mPTP onset but does not affect δTR amplitude.

(A-C) Analysis of mPTP opening by measuring mitochondrial swelling via determination of the delta-thinness ratio (δTR). (A) An example of δTR determination. COS-7 cells were transfected two days prior to analysis with an RFP targeted to mitochondria. Cells were treated with calcimycin for 120 min, as indicated by the solid horizontal line, to induce mPTP opening. Red and blue dashed lines indicate the average δTR values before and after the onset of mPTP opening, respectively. Vertical double-headed arrow indicates the amplitude of δTR . Horizontal double-headed arrow indicates the time from the addition of calcimycin to the onset of mPTP opening. (B, C) COS-7 cells were transfected two days prior to analyses with an RFP targeted to mitochondria, together with empty vector (control, blue), 11B (light magenta), 11A220 (dark magenta) and 11B+11A220 (green). (B) Quantification of the time from the addition of calcimycin to the onset of mPTP opening. Each dot represents one individual cell analyzed. Horizontal lines indicate the mean. (C) Quantification of the δTR amplitude. Error bars, SD; *, $P < 0.05$; N.S., not statistically significant.

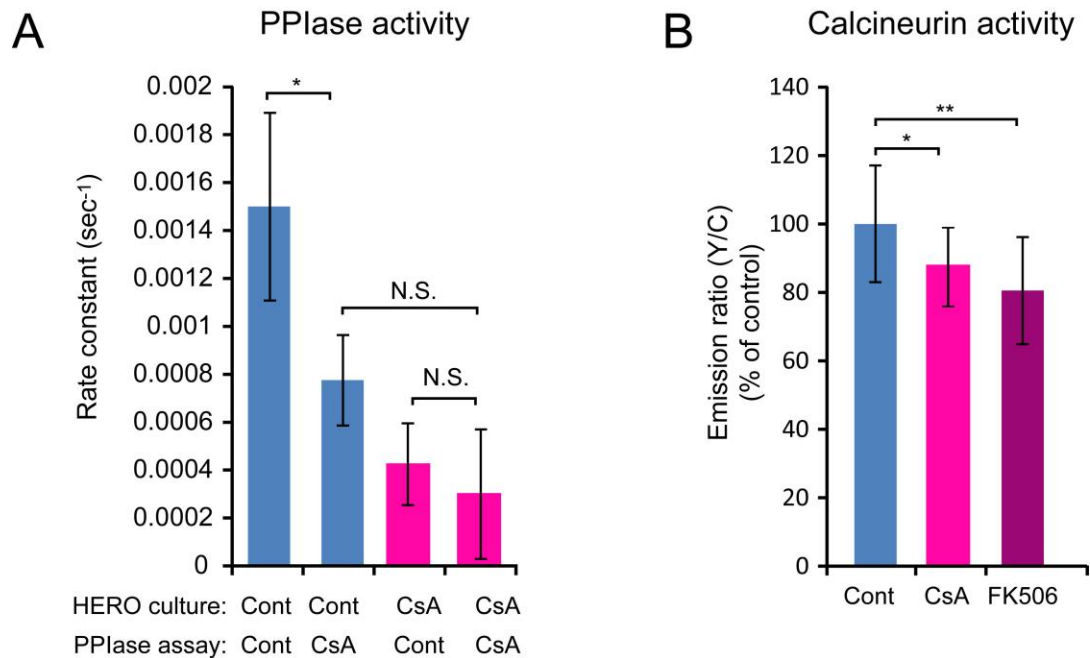


Figure S4. Validation of CsA and FK506 effects in mouse neocortex.

(A) Peptidylprolylisomerase (PPIase) activity assay. Mouse E13.5 cerebral hemispheres were subjected to HERO culture for 24 h without (control; Cont) or with 4 μ M cyclosporin A (CsA). A 5,000 g supernatant prepared from the tissue was then subjected to the PPIase assay under the control condition (Cont) or in the presence of 5 μ M CsA. Zero-order rate constants are indicated on the ordinate axis.

(B) Calcineurin activity assay. Mouse E13.5 neocortex was subjected to IUE with the FRET-based calcineurin activity sensor Cyto-CaNAR2, followed by HERO culture for 24 h without (control, Cont) or with 4 μ M cyclosporin A (CsA) or FK506. Hemisphere slices were then subjected to Cyto-CaNAR2-based FRET imaging. Yellow and cyan (Y/C) emission ratios relative to control (set to 100%) are indicated on the ordinate axis.

Error bars, SD; **, $P < 0.01$; *, $P < 0.05$; N.S., not statistically significant.

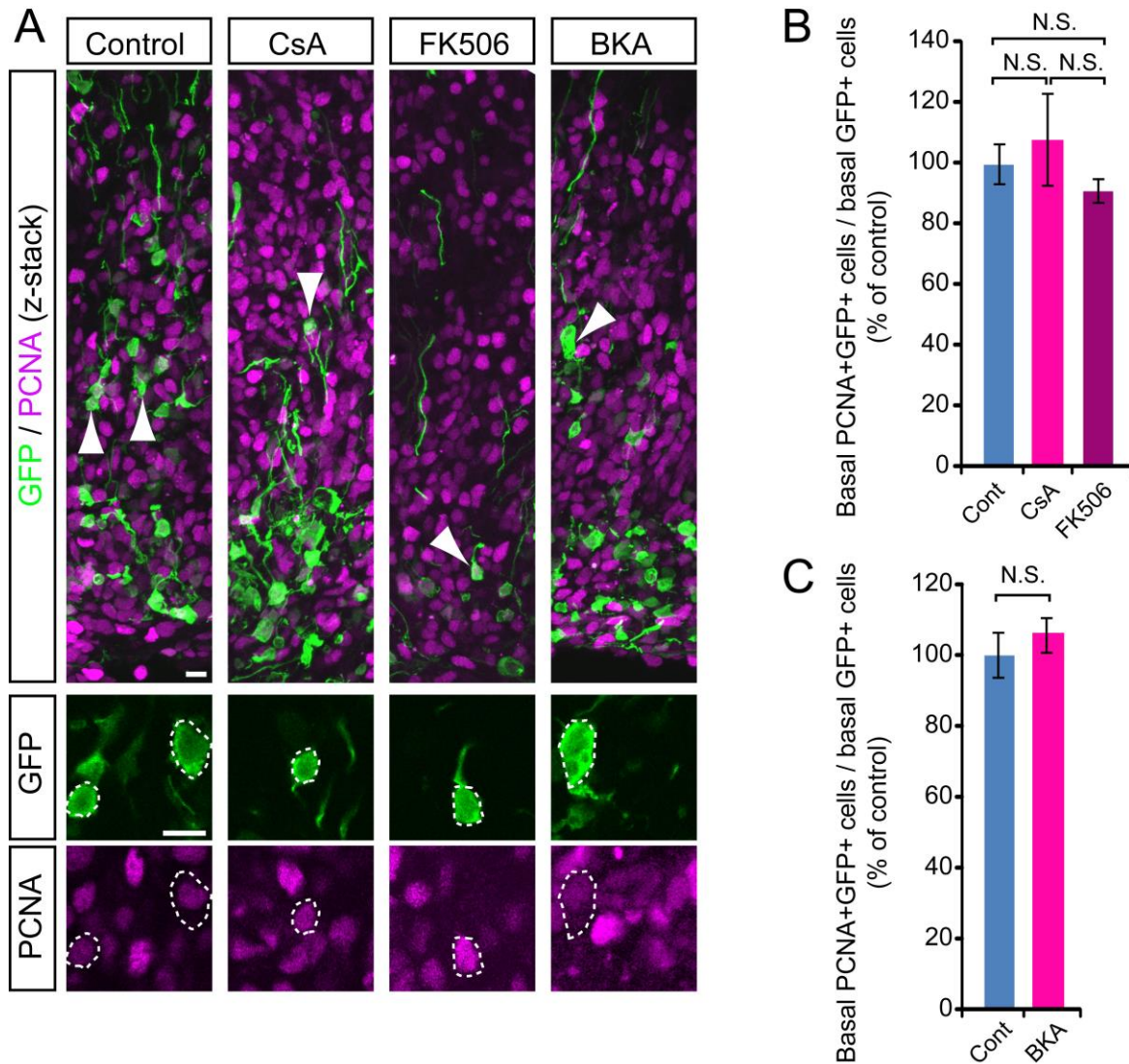


Figure S5. Lack of effect of CsA, FK506 and BKA on BP abundance in human neocortex.

5 Neocortical tissue of human PCW11-13 fetuses was electroporated with EGFP and subjected to FFT culture for one day without treatments. Tissue was then further cultured for 2 days in the absence (Control, Cont) or presence of 4 μ M cyclosporin A (CsA), 4 μ M FK506 or 20 μ M bongkreikic acid (BKA). (A) GFP (green) and PCNA (magenta) double immunofluorescence of PCW11 neocortex. Bottom panels, high magnification of the cells (dashed circles) indicated by arrowheads in the top panels, showing either the GFP or PCNA immunofluorescence; all cells

shown are PCNA⁺ GFP⁺. **(B, C)** Quantification of basal GFP⁺ cells that are PCNA⁺, with treatments as indicated. The mean values for the controls were set to 100%, and the mean values for the indicated treatments are expressed relative to these.

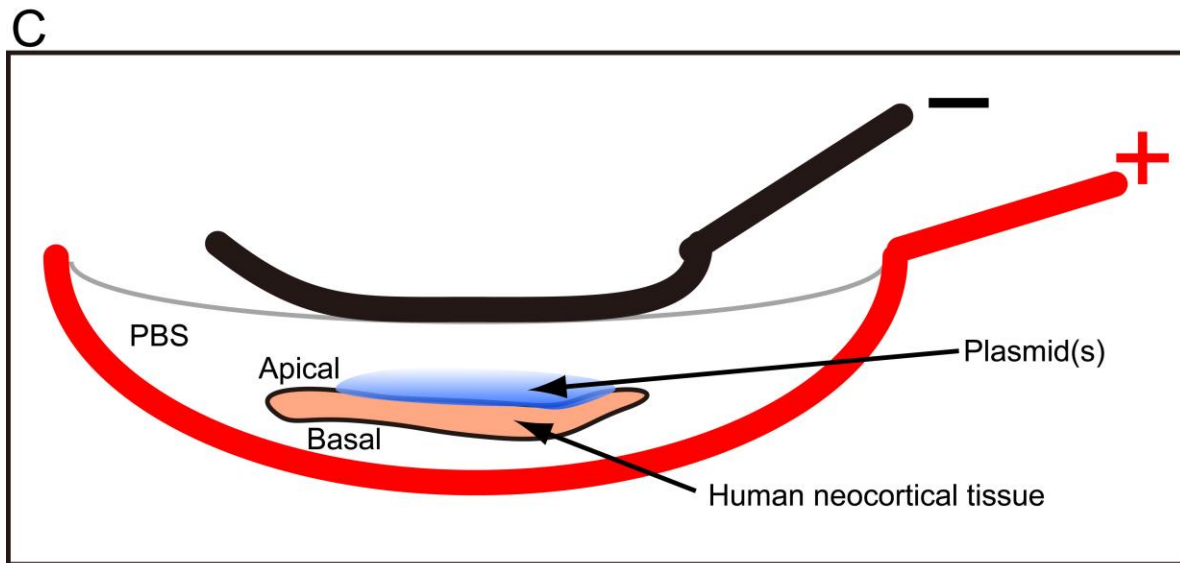
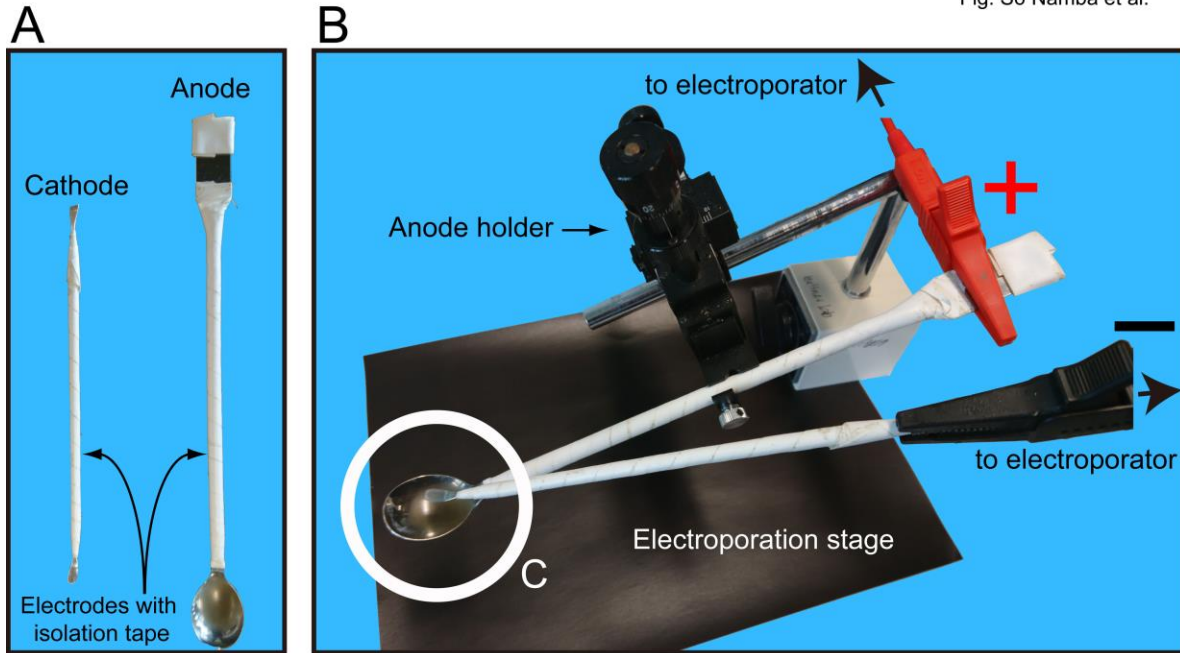


Figure S6. A novel electroporation system for fetal human neocortical tissue ex vivo.

(A) Stainless steel laboratory spatulas are wrapped with an isolation tape and used as electrodes. The small spatula is used as cathode and the larger, spoon-shaped spatula as anode.

5 (B) Setup of the electroporation system. The electroporation stage consists of the spoon-shaped anode (+) spatula that is fixed to the anode holder. The cathode (-) is held by the operator's hand. Both anode and cathode are connected to the electroporator. A schematic image of the electrode region indicated by the white circle is shown in C.

10 (C) Schematic cross-section image of the electrodes. Fetal neocortical tissue is placed onto the spoon-shaped anode (+, red) filled with sterile PBS. Plasmid(s) is/are added onto the apical surface of the tissue. The cathode (-, black) is placed on top of the PBS-covered tissue, and electroporation is performed. Plasmid DNA enters the cells in the apical-to-basal direction.

(D) Neocortical tissue of human PCW11 fetus was electroporated with EGFP and subjected to FFT culture for 72 h. The bright field and GFP fluorescence images were acquired from the apical side of the tissue.

KEY RESOURCES TABLE

REAGENT or RESOURCE	SOURCE	IDENTIFIER
Antibodies		
anti-ARHGAP11A	Abcam	Cat#ab113261; RRID:AB_10866587
anti-ARHGAP11B	This Paper	3758-A37-5
anti-FLAG	Sigma	Cat#F1084
anti-GFP	MPI-CBG	N/A
anti-HA	Cell Signaling Technology	Cat#3724
anti-GFP	Abcam	Cat#ab290; RRID:AB_303395
anti-GFP	Roche	Cat#1867423
anti-PCNA	Milipore	Cat#CBL407; RRID:AB_93501
anti-PH3	Abcam	Cat#ab10543; RRID:AB_2295065
anti-SOX2	Santa Cruz Biotechnology	Cat#SC-17320; RRID:AB_2286684
anti-Tbr2	This Paper	3815-A12-1
anti-Tbr2	Robert Hevner	Englund et al., 2005
anti-TOM20	Abcam	Cat#ab56783; RRID:AB_945896
anti-TOM20	Abcam	Cat#ab78547; RRID:AB_2043078
anti-TOM20	Santa Cruz Biotechnology	Cat#SC-11415; RRID:AB_2207533
anti-goat IgG-Alexa Fluor 488	ThermoFisher Scientific	Cat# A11055; RRID:AB_2534102
anti-goat IgG-Alexa Fluor 647	ThermoFisher Scientific	Cat# A21447; RRID:AB_2535864
anti-mouse IgG-Alexa Fluor 488	ThermoFisher Scientific	Cat#A21202; RRID:AB_141607
anti-mouse IgG-Alexa Fluor 555	ThermoFisher Scientific	Cat#A31570; RRID:AB_2536180
anti-mouse IgG-Alexa Fluor 647	ThermoFisher Scientific	Cat#A31571; RRID:AB_162542
anti-mouse IgG-HRP	Jackson ImmunoResearch	Cat#115-035-068; RRID:AB_2338505
anti-rabbit IgG-Alexa Fluor 488	ThermoFisher Scientific	Cat#A21206; RRID:AB_2535792
anti-rabbit IgG-Alexa Fluor 647	ThermoFisher Scientific	Cat#A31573; RRID:AB_2536183
anti-rabbit IgG-HRP	Jackson ImmunoResearch	Cat#711-035-152; RRID:AB_10015282
anti-rat IgG-Alexa Fluor 488	ThermoFisher Scientific	Cat#A21208; RRID:AB_2535794
normal mouse IgG	Jackson ImmunoResearch	Cat#015-000-003; RRID:AB_2337188
normal rat IgG	Abcam	Cat#ab326
Biological Samples		
PCW10-11 human brain tissue	Uniklinikum Dresden	N/A
PCW10-14 human brain tissue	HDBR	N/A
Chemicals, Peptides, and Recombinant Proteins		
GST-11B	This Paper	N/A
GST-11A220	This Paper	N/A

MBP-ANT2	This Paper	N/A
α -chymotrypsin	Sigma	Cat#C7762
N-succinyl-Ala-Ala-Pro-Phe- <i>p</i> -nitroanilide	Sigma	Cat#S7388
Cyclosporin A	Sigma	Cat#30024
FK-506 monohydrate	Sigma	Cat#F4679
Bongkreic acid . triammonium salt	Enzo Life Science	Cat#BML-CM113
2-Deoxy-D-glucose	Sigma	Cat#D8375
6-diazo-5-oxo-L-norleucine	Sigma	Cat#D2141
BPTES	Sigma	Cat#SML0601
2,4-Dinitrophenol	Sigma	Cat#34334
GST-ARHGAP11B221-267	This Paper	N/A
Critical Commercial Assays		
Seahorse XF Real-Time ATP Rate Assay Kit	Agilent	Cat#103592-100
Seahorse XFe96 Flux Paks	Agilent	Cat#102601
Mouse Neuron Nucleofector® Kit	Lonza	Cat#VVPG-1001
Experimental Models: Cell Lines		
NHI-3T3	MPI-CBG	N/A
COS-7	MPI-CBG	N/A
Experimental Models: Organisms/Strains		
C57BL/6J	MPI-CBG	N/A
Recombinant DNA		
pCAGGS-ARHGAP11B Δ 2-21	This Paper	N/A
pCAGGS-ARHGAP11B Δ 2-12	This Paper	N/A
pCAGGS-mSlc25a5	This Paper	N/A
pCAGGS-ARHGAP11A220-HA	This Paper	N/A
pCAGGS- ARHGAP11A250 -HA	This Paper	N/A
pCAGGS-ancARHGAP11B-NLS-mt-HA	This Paper	N/A
pEGFP-N3-ARHGAP11B1-30	This Paper	N/A
pGEX-6P-ARHGAP11A220	This Paper	N/A
pGEX-6P-ARHGAP11B221-267	This Paper	N/A
pGEX-6P-ARHGAP11B	This Paper	N/A
pCMV-mSlc25a5-3xFLAG	This Paper	N/A
pOCC102-mSlc25a5	This Paper	N/A
pCAGGS-ancARHGAP11B-HA	Florio et al., 2016	N/A
pCAGGS-EGFP	Florio et al., 2015	N/A
pDsRed2-Mito	Clontech	Cat#632421
pCAGGS-ARHGAP11B-HA	This Paper	N/A
pCAGGS	Florio et al., 2015	N/A
p3XFLAG-CMV-14	Sigma	Cat#E7908

pGEX-6P-1	Promega	N/A
pCAGGS-ARHGAP11A	This Paper	N/A
pCAGGS-ARHGAP11B	Florio et al., 2015	N/A
pCAGGS-HA-ARHGAP11B	Florio et al., 2016	N/A
pCAGGS-ARHGAP11A220	This Paper	N/A
Software and Algorithms		
SigmaPlot	Systat Software	N/A
ZEN	Zeiss	N/A
Fiji	http://fiji.sc	RRID:SCR_002285
Image Analyst MKII	Image Analyst Software	N/A
MetaMorph 6.0	Molecular Devices	N/A
MASCOT	50 Matrix Sciences Ltd	version 2.2.04
Scaffold	Proteome Software	v.4.8.7
Excel	Microsoft	RRID:SCR_016137
Statcel3	OMS	RRID:SCR_016753
MYSTAT	Systat Software	N/A